The University of Adelaide

Master of Philosophy (Physical Science)

Thesis

Project:

Optical fibre cavities for sensors and lasers

Liushun Xie

Faculty of Sciences

School of Physical Sciences

Supervisors:

Heike Ebendorff-Heidepriem

Stephen C. Warren-Smith and Linh V. Nguyen

20 March 2020

Contents

List of Publications

Journal papers

Published:

L. Xie, L. V. Nguyen, H. Ebendorff-Heidepriem, and S. C. Warren-Smith, “Multiplexed optical fiber biochemical sensing using cascaded C-shaped Fabry-Perot Interferometers,” *IEEE Sensor Journal,* vol. 19, no. 22, pp. 10425-10432, 2019.

Accepted:

X. Li, S. C. Warren-Smith, L. Xie, H. Ebendorff-Heidepriem, L. V. Nguyen, “Temperature-compensated refractive index measurement using a dual Fabry–Perot interferometer based on C-fiber cavity,” *IEEE Sensor Journal,* 2020.

Conference papers

Published:

L. Xie, L. V. Nguyen, H. Ebendorff-Heidepriem, and S. C. Warren-Smith, "Interferometric multiplexed fiber sensing using C-shaped fibre," The Australian Conference on Optical Fibre Technology, Perth, 2018.

Submitted:

X. Li, L. Xie, S. C. Warren-Smith, H. Ebendorff-Heidepriem, and L. V. Nguyen, " Simultaneous temperature and refractive index sensing using C-fibre Fabry-Perot microcavity," The 14th Pacific Rim Conference on Lasers and Electro-Optics, Sydney, 2020.

Abstract

Specialty optical fibres provide opportunities for light-matter interactions using nanolitre samples. In this thesis, optical microcavities using specialty fibre have been fabricated and tested for both sensing and laser applications.

Optical fibre sensors with multiplexing ability are proposed and demonstrated based on Fabry-Pérot interferometers formed by serially splicing C-shaped fibre between single mode optical fibres. The multiplexing ability is demonstrated by filling different NaCl solutions into the separate cavities in a dual cavity system. Demultiplexing is achieved using Fourier techniques and the results show minimal crosstalk between the two interferometers. The dual-cavity interferometric sensor was then applied to biochemical sensing by utilizing polyelectrolyte layer by layer self-assembly followed by the biotin-streptavidin binding mechanism. The proposed sensor solves an important problem in biochemical sensing by providing an ability to simultaneously measure a negative control, critical for reducing false positive measurements. This work was published in IEEE Sensors Journal and was presented at the 2018 Australian Conference on Optical Fibre Technology.

The second part of the thesis describes the use of C-shaped fibres and exposed core microstructured optical fibres to create a microfluidic dye laser. The aim is to create a single transverse mode fibre laser with visible wavelength emission using microfluidics to solve the problem of photobleaching of dye lasers. The C-shaped fibre dye laser is based on a Fabry-Pérot cavity while the exposed core fibre provides a mechanism to operate with a guided mode where the evanescent field can interact with the gain medium. In both cases, the optical pumping was achieved using a pulsed Nd:YAG laser at 532 nm and the gain medium is rhodamine B solution. An analysis of the feasibility of both approaches is given as well as preliminary results.

Declaration

I certify that this work contains no material which has been accepted for the award of any other degree or diploma in my name, in any university or other tertiary institution and, to the best of my knowledge and belief, contains no material previously published or written by another person, except where due reference has been made in the text. In addition, I certify that no part of this work will, in the future, be used in a submission in my name, for any other degree or diploma in any university or other tertiary institution without the prior approval of the University of Adelaide and where applicable, any partner institution responsible for the joint-award of this degree.

I acknowledge that copyright of published works contained within this thesis resides with the copyright holder(s) of those works.

I also give permission for the digital version of my thesis to be made available on the web, via the University's digital research repository, the Library Search and also through web search engines, unless permission has been granted by the University to restrict access for a period of time.

Signed:

Date:

20.03.2020

Acknowledgement

I want to acknowledge my supervisors, Prof. Heike Ebendorff-Heidepriem, Dr. Stephen Warren-Smith and Dr. Linh Nguyen, for their constant support and guidance. The discussions between us have help me understand much not only about my projects but also about the whole optics. The results of this thesis would not have been possible without their supervision and contribution. Heike provided much general guidance on the direction of the projects and helped me much in finding problems and solutions. Stephen and Linh supported me much in both theoretical and experimental aspects. Their enthusiasm and skills have been significant in the whole research process. It has been a great pleasure to work with them for the last two years.

I also want to acknowledge the optical fibre group at the Institute for Photonics and Advanced Sensing of the University of Adelaide. The regular meetings of the group have been very fruitful and inspired many wonderful ideas. The whole group also helped me to diagnose the issues and to find solutions. Particularly, I want to acknowledge Lu Peng and Xuegang Li for their support. We have been working together for long time and our discussions are very beneficial.

I acknowledge the Institute for Photonics and Advanced Sensing for providing the lab for experiments, the Optofab node of the Australian National Fabrication Facility for funding and experimental equipment. I would like to acknowledge Evan Johnson and Alastair Dowler for their contribution to the fibre fabrication..

Chapter 1 Introduction

The research presented in this thesis focuses on developing optical fibre sensors and fibre lasers with specialty fibres such as C-shaped fibres and exposed core optical fibres. In this chapter, the general knowledge of optical fibres is firstly introduced in terms of materials, fabrication and theory. After that, several kinds of specialty fibres that have been developed for sensors and lasers are introduced. In the end, different techniques applied in optical fibre sensors and lasers are concluded.

1.1 Optical fibre overview

1.1.1 General fibre introduction

Optical fibres refer to a class of cylindrical waveguides constructed with different refractive index (RI) optical materials, typically glass, for light propagation. Since Kao and Hockham [1] first theoretically proposed that losses below 20dB/km can be achieved by removing glass impurities, optical fibres have been studied and applied in telecommunication, sensing, and imaging due to their advantages such as low loss transmission, electromagnetic immunity and chemical stability. Normally, an optical fibre incorporates core and cladding. By properly adjusting the refractive index profile, light can be guided inside the core based on total internal reflection (TIR). Specifically, the refractive index of the core, n_1, is made higher than the refractive index in the cladding n_2. If the incident angle of the incoming light, θ_{in}, is less than the critical angle of the fibre, θ_c (1), as shown in Fig. 1, then the light will be confined to the optical fibre core.

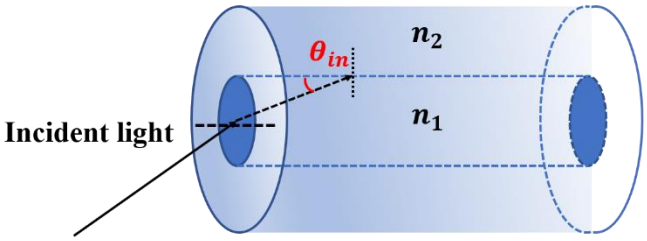

Fig. 1: The principle of total internal reflection.

$$\sin\theta_c = \frac{n_2}{n_1} \tag{1}$$

The most commonly used fibres are step-index fibres (SIF) and graded index fibres (GIF). They are classified by the RI distribution in the core. Besides step index fibres and graded index fibres, optical fibres can also be classified by the supporting propagation modes inside them, specifically, single mode fibres (SMF) and multimode fibres (MMF). The description of fibre modes will be provided later. Fig. 2 shows the RI profile of (a) a step index single mode fibre, (b) a step index multimode fibre and (c) a graded index multimode fibre.

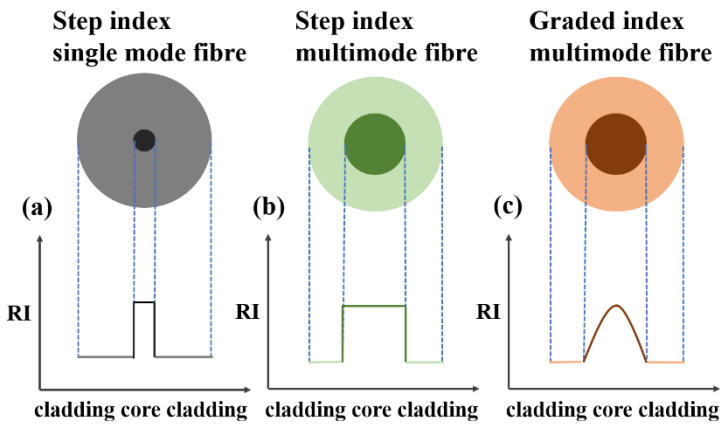

Fig. 2: Fibre geometry and RI profile of (a) step index single mode fibre and (b) step index multimode fibre and (c) graded index multimode fibre.

A. Materials

Many optical materials have been used for optical fibre fabrication, with silica glass being the most commonly used material. Higher RI in the core is normally obtained by doping the silica glass with chemicals such as GeO_2. The lowest transmission loss ever achieved for silica fibre is 0.154 dB/km [2] at a transmission wavelength of 1550nm. In this case, the signal power reduces to half of the original signal after propagating for 20 km. Other materials such as polymers and soft glasses are also utilized to provide different optical characteristics. For example, polymer optical fibre normally can provide greater bending and stretching ability [2].

B. Fabrication

Fabrication of optical fibres typically involves two steps, being preform fabrication and fibre drawing. An optical fibre preform is normally a cylindrical rod (centimetre scale in diameter and about half meter long) with the designed RI profile in the core and cladding. It has the same optical characteristics such as attenuation but in a much larger scale. A preform can be made from vapour deposition, micromachining, extrusion or even 3D printing [2]. After the preform fabrication, the cylindrical rod is then drawn to optical fibre the desired diameter, typically 80-200 μm, using a fibre drawing tower.

C. Theory

The light propagating inside an optical fibre can be described by Maxwell's equations (2-5) for a non-conducting isotropic medium [2].

$$\nabla \cdot \vec{E}=0 \tag{2}$$

$$\nabla \cdot \vec{B}=0 \tag{3}$$

$$\nabla \times \vec{\mathrm{E}}=-\frac{\partial \vec{B}}{\partial t} \tag{4}$$

$$\nabla \times \vec{\mathrm{B}}=\mu\varepsilon \frac{\partial \vec{E}}{\partial t} \tag{5}$$

where $\boldsymbol{E}$ is the electric field; $\boldsymbol{B}$ is the magnetic field; μ is the permeability and ε is the permittivity of the medium. Then the electromagnetic fields under the boundary conditions can be expressed as [2]:

$$\nabla_t^2 E_z + [(\frac{\omega n}{c})^2 - \beta^2] \cdot E_z = 0 \tag{6}$$

$$\nabla_t^2 H_z + [(\frac{\omega n}{c})^2 - \beta^2] \cdot H_z = 0 \tag{7}$$

where E_z and H_z are the electric and magnetic field in the z direction; t subscript represents the transverse direction; ω is the frequency of the light; β is the phase constant; n is the RI of the medium and c is the light speed in free space. In step index fibres, there are three classes of guided modes: transverse electric modes (TE modes, E_z=0), transverse magnetic modes (TM modes, H_z=0) and transverse electromagnetic modes (TEM modes, $E_z \neq 0$, $H_z \neq 0$). In weakly guiding fibre where the RI contrast between core and cladding is very small ($n_1 \approx n_2$), the so-called weak-guidance approximation can be used and resulting modes are designated as linearly polarised modes (LP modes). In this case, the field is nearly a plane wave and $E_x \approx \eta H_y$ where $\eta=\eta_0/n_2$. The corresponding fields under cylindrical coordinates (r, ϕ, z) can be expressed as:

$$E_x = \begin{cases} AJ_l(\frac{ur}{a})\cos(l\phi)\exp(-i\beta z), & \text{r} \le \text{a} \\ CK_l(\frac{wr}{a})\cos(l\phi)\exp(-i\beta z), & \text{r} \ge \text{a} \end{cases} \quad (8)$$

$$H_y = \begin{cases} BJ_l(\frac{ur}{a})\cos(l\phi)\exp(-i\beta z), & \text{r} \le \text{a} \\ DK_l(\frac{wr}{a})\cos(l\phi)\exp(-i\beta z), & \text{r} \ge \text{a} \end{cases} \quad (9)$$

$$u = a\sqrt{k^2 n_1^2 - \beta^2} \quad (10)$$

$$w = a\sqrt{\beta^2 - k^2 n_2^2} \quad (11)$$

where l is angular mode number related to the LP modes; a is the radius of the core; K and J are Bessel functions; k is wavenumber; β is the phase constant; u and w are the normalised transverse wavenumber; A, B, C and D are coefficients related to the solutions of the Bessel functions, specifically, $A \approx \eta B$ and $C \approx \eta D$. From (8) and (9), the electric field and magnetic field will extend into the cladding, which is referred to as the evanescent field. The intensity of evanescent field decreases exponentially into the cladding and the penetration depth is normally about several hundred nanometres to several microns depending on fibre types. For example, the penetration depth of suspended core fibres is about tens of nanometres up to 100 nanometres. The evanescence field is significant for optical fibre sensing as it can be used as a means to interact with the external environment.

Two critical parameters for an optical fibre are core radius and RI difference between the core and cladding. The dimensions of these two parameters, along with the wavelength of the propagating light, will determine whether the optical fibre is single mode or multimode. Normally, the core radius of single mode fibre is between 8 to 10 μm and the core radius of multimode fibre is between 50 to 200 μm. Fig. 3 shows the field distribution simulation (COMSOL 5.4) of the fundamental mode supported by an 8 μm core SMF and a selected higher order mode supported by an 50 μm core MMF.

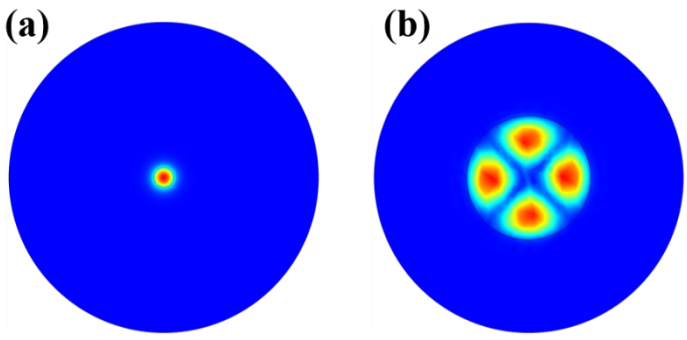

Fig. 3: (a) Fundamental mode of SMF and (b) LP21 mode for MMF.

To describe the RI difference and justify the maximum light acceptance angle of a fibre, numerical aperture (NA) is introduced, which is given by:

$$NA = \frac{1}{n_0}\sqrt{n_1^2 - n_2^2} \tag{12}$$

where n_0 is the RI of surrounding medium (equal to 1 in the case of air). Note that this equation only applies when the RI contrast is small.

Besides the core diameter and NA, another parameter to distinguish single mode fibres from multimode fibres is the V-number, which is defined as:

$$V = \frac{2\pi}{\lambda} \cdot a \cdot \sqrt{n_1^2 - n_2^2} \tag{13}$$

It is determined by the core RI n_1, cladding RI n_2 and the core radius a. Calculated from the wave equation, the cut-off value of V between single mode fibre and multimode fibre is about 2.405. For multi-mode fibres, the number of modes can be estimated as:

$$N \approx \frac{V^2}{2} \tag{14}$$

Step index SMFs and MMFs are the most utilised fibres in optical communication. However, significant efforts have been put into developing specialty fibres for other applications such as sensing and imaging.

1.1.2 Specialty fibres

Since the demonstration of the first optical fibre, many classes of specialty fibres have been demonstrated for various applications such as sensing, imaging and laser generation. For example, the C-shaped fibre can help facilitate the interaction of light with gases and liquids for sensing. D-shaped fibres and some microstructured fibres such as exposed core fibre and suspended core fibre can be utilised for sensing through interaction with the evanescent field. In addition, photonic crystal fibres have been applied in many applications such as sensing and lasing. These specialty fibres are discussed individually in the following paragraphs.

A. C-shaped fibre

A C-shaped fibre or C-shaped cavity is a kind of hollow core capillary that has a C-shaped cross-section as shown in Fig. 4.

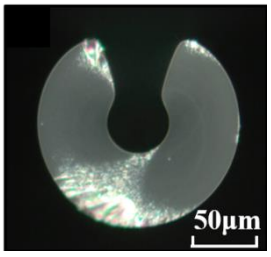

Fig. 4: Cross-section image of a C-shaped fibre

The inner and outer diameter for a C-shaped fibre is normally comparable to common optical fibres so that it can be embedded as a sensing spacer into two optical fibres. The C-shaped fibres are not optical waveguides, but the presence of the C-shape fibres can facilitate the interaction between light path and measurand. Compared to traditional fibres such as SMF or MMF, the C-shaped fibre offers an opportunity for the liquid or gas to directly interact with the light field. In this case, any changes in the optical path such as the RI or temperature can be captured by monitoring the light propagating within the cavity. When the length of the C-shaped fibre is short enough, the divergence within the cavity can be neglected, which is suitable for interferometric sensors. A C-shaped fibre is normally fabricated through milling or drilling on the preform. The sensors formed by C-shaped fibres have been used in temperature, RI and biochemical sensing [3, 4] in recent years.

B. D-shaped optical fibre

D-shaped optical fibre is a kind of side-polished optical fibre with a core close to the polished surface in which the evanescence field can extend into the sensing area as shown in Fig. 5. By applying changes to the surrounding measurands, the D-shaped fibre may be utilised for temperature [5], strain [6] or RI sensing [7]. With further treatment such as depositing metal films on the polished side, the D-shaped fibres can be utilised to generate surface plasmon wave for sensing [5, 8] or to form a polarizer [9]. The D-shaped fibres are normally fabricated by side polishing. Other methods such as femtosecond laser machining [10] can also be applied into D-shaped optical fibre fabrication.

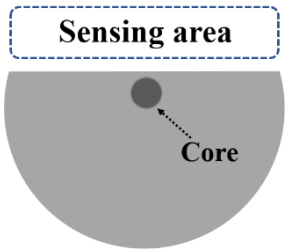

Fig. 5: Cross-section of a D-shaped optical fibre.

C. Photonic crystal fibre

In recent years, photonic crystal fibres (PCFs) have been intensively studied [11].The guidance mechanism of PCF can be divided into two main classes: index-guiding PCFs and photonic bandgap PCFs [12, 13]. In the index-guiding PCF as shown in Fig. 6 (a), a solid core is surrounded by air holes which reduce the effective RI of the cladding. As a result, the effective RI of core is larger than that of the cladding so that light can be guided in the PCF by the principle of total internal reflection. In Fig. 6 (b), a hollow core is surrounded by air holes which create a photonic bandgap in the cladding area. The light can then be guided in the bandgap for a specific wavelength range. The PCFs are normally fabricated by arranging a periodical RI distribution in the core area such as stacking [14] of glass tubes during preform fabrication.

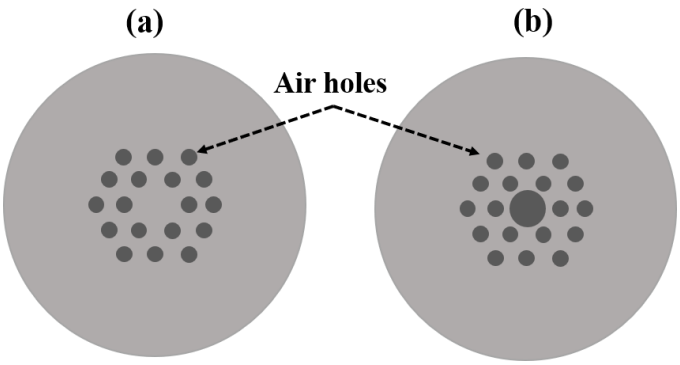

Fig. 6: Cross-sectional configuration of PCF based on (a) index-guiding and (b) photonic bandgap.

PCFs have been used for many applications from constructing lasers [15] to sensing [16]. For instance, Dudley *et al.* demonstrated supercontinuum generation using PCF in 2005 [17]. As chemical sensors, PCFs have been used for highly sensitive RI sensing with a sensitivity of 30,100 nm/RIU developed by Wu *et al.* [18]. As biosensors, Jensen *et al.* [19] applied PCFs for evanescence field based sensing of fluorophore-labelled biomolecules by filling the air holes with aqueous solutions. Other biochemical sensing applications can be found in Refs. [20, 21].

D. Suspended core fibre and exposed core fibre

Suspended core fibres (SCF) and exposed core fibres (ECF) are both microstructured optical fibres that can be used for sensing through us of their evanescence field. Their cross-sectional images are shown in Fig. 7. The suspended core fibres consist of three air holes and a small core area formed by these air holes. Due to the high RI contrast, the suspended core fibres are normally multimoded fibres. By filling liquid or gas into the air holes, suspended core fibres can be used for biosensing and chemical sensing. Compared with suspended core fibres, exposed core fibres have an open side so that the core is exposed to the external environment directly. The structure of the ECF makes the sensing process easier as measurands can reach the core directly. The SCF and ECF have been successfully applied in temperature sensing [22], fluorescence sensing [23, 24], biosensing [25], and RI sensing [26].

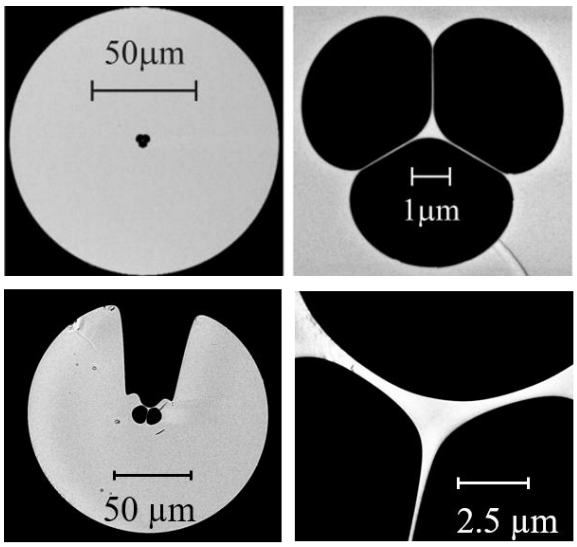

Fig. 7: Cross section images of suspended core fibre [27] and exposed core fibre [23].

1.2 Optical fibre chemical and biological sensing overview

Optical fibre sensing has great potential in many applications due to its advantages such as small size, immunity to electromagnetic interference, and high sensitivity. Various techniques have been studied such as fibre grating sensors, evanescent-field sensors and interferometric sensors. Optical fibres can also be used to achieve distributed sensing through techniques such as distributed temperature sensing based on Raman scattering and distributed acoustic sensing (DAS) based on Rayleigh scattering, which are well studied and have been transferred to practical applications. Based on these fibre sensing techniques, some integrated systems have been applied in military, civil engineering and security systems. In biosensing and chemical sensing area, sensing techniques such as fibre grating sensors, surface plasmon resonance sensors and interferometric sensors are widely used for their own outstanding features in many aspects. These techniques will now be discussed in terms of advantages and disadvantages when used for sensing.

1.2.1 Optical fibre grating sensors

Gratings have been widely used for optical fibre sensing. Fibre gratings are fabricated by inducing periodic RI distribution into the fibres. For instance, Hill *et al.* [28] firstly fabricated a fibre Bragg grating (FBG) using internal laser writing in 1978. This method is based on launching high intensity laser light into fibres and induce RI distribution. In addition, Meltz *et al.* [29] then successfully made a grating through holographic techniques in 1989 which showed great potential to produce lower cost gratings. Most fibre gratings used for telecommunication and fibre sensing are fabricated by exposing the fibre covered with a phase mask to UV light. In recent decades, the research interests for fibre grating fabrication have turned to femtosecond laser machining, which can create gratings in non-photosensitive glass with a high degree of flexibility. There are many types of fibre gratings that have been introduced such as fibre Bragg grating (FBG) [30], long-period fibre grating [31], chirped fibre grating [32], titled fibre grating [33] and sampled fibre grating [34].

Among them, FBGs are the most mature technique for use as a fibre sensor element. Under certain phase matching conditions, an FBG couples the forward propagating core modes to the backward propagating core modes. Fig. 8 demonstrates a typical FBG.

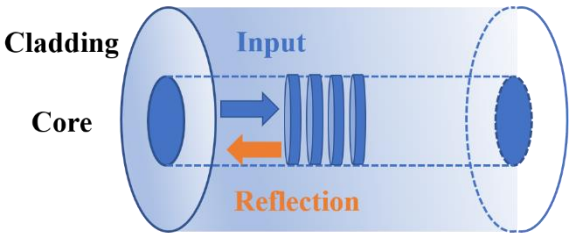

Fig. 8: Schematic diagram of an FBG.

For simplicity, consider the case of broadband light coupled into the FBG written on a single mode fibre. A discrete wavelength will be reflected, called the Bragg wavelength, which is determined by the grating period Λ and effective RI n_{eff} as shown in Fig. 8. This relationship

can be expressed as:

$$\lambda = 2n_{eff}\Lambda \tag{15}$$

Giles [35] introduced the optical sensing application of FBG in 1997. In most situations, the FBG sensors are utilized for strain sensing and temperature sensing with the help of FBG interrogators. For strain sensing, the applied strain changes the grating period, which can cause the change of reflected Bragg wavelength. For temperature sensing, the effective RI is changed by temperature change due to the thermo-optic effect. The use of an FBG interrogator can help obtain measurand information from the reflected light signal such as wavelength change. Recently, many researchers applied FBGs for biosensing applications. Chryssis *et al*. [36] successfully used FBG to detect DNA hybridization based on an etched FBG. Sridevi *et al.* [37] utilized the FBG biosensor for C-reactive protein detection. In addition, Libish *et al*. [38] performed protein concentration measurement based on FBG sensors using a DNA coating. Traditional FBG sensors are not the most suitable technique for biosensors and chemical sensors as most FBGs are written inside the core of fibres where the measurands cannot directly reach. A promising approach is the use of microstructured optical fibres where measurands can directly interact with the optical field. For example, Warren-Smith and Monro [39] fabricated an FBG onto a silica exposed core microstructured fibre where chemicals can contact the core directly through a side opening.

1.2.2 SPR (Surface plasmon resonance)-based fibre sensors

Surface plasmon resonance is a sensitive technique for RI sensing and biochemical sensing, which utilises surface electromagnetic waves that propagate between a thin metal film and a dielectric substrate. This can be the core of an optical fibre in the case of fibre sensing. The SPR is based on charge density oscillation of the metal material. The first SPR-based optical fibre sensor was demonstrated by Jorgenson and Yee [40] by symmetrically depositing 550 Å silver film onto a short piece of cladding-removed fibre. When a thin (nanoscale) metal film is deposited on the surface of an optical fibre core, the evanescence wave of the fibre excites the surface plasmon under certain phase-matching conditions, which leads to surface plasmon waves propagating in the metal-fibre interface with a direction into the dielectric materials as shown in Fig. 9.

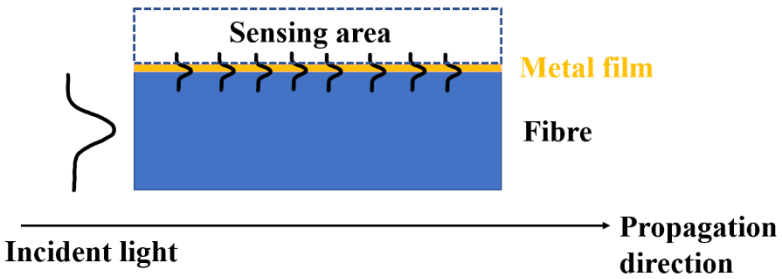

Fig. 9: Schematic diagram of SPR.

The surface plasmon wave on the interface will decay into the metal and fibre core

exponentially. The resonance condition can be adjusted to be highly sensitive to the refractive index of the external sensing area. This property can be utilised for sensing by altering the interface conditions such as exposing the metal film with different chemicals and biological materials. Chau *et al.* [41] applied SPR-based optical fibre sensors into Ni^{2+} sensing and label-free detection of streptavidin and staphylococcal enterotoxin B. Hassani and Skorobogatiy [40, 42] designed a microstructure optical fibre for SPR sensing, which can be potentially used for biochemical sensing if combined with micro-fluidic techniques. SPR fibre-based sensors are normally flexible and small with good performance in resolution and sensitivity, however, controlling the metal coating consistency is challenging and the resonance bandwidth can be quite broad leading to relatively poor precision.

1.2.3 Interferometric optical fibre sensors

An interferometer is based on light interference. The main principle is that two coherent light paths with the same frequency and polarisation will interfere leading to an interference spectrum according to their super-position. Many interferometer-based techniques have been embedded with optical fibres such as Sagnac, Mach-Zehnder, Michelson and Fabry-Pérot interferometers. Among them, Fabry-Pérot interferometers and Sagnac interferometers are two main optical fibre interferometric sensors that have been widely used for their applications in biochemical sensing.

A. Sagnac interferometric sensors

The principle of optical Sagnac interferometer is based on Sagnac effect or Sagnac interference introduced by Georges Sagnac in 1913. Fig. 10 demonstrates the principle of a general Sagnac interferometer. The light transmitted into the beam splitter will generate two light beams with the same properties (i.e. same polarization and phase) but the opposite transmission direction. Because of the rotation applied on the loop, these two beams will end up with different optical path. Specifically, the light with the same propagating direction as the rotation will go through longer optical path than the light with opposite direction. The optical path length will induce a phase difference between the two light beams and lead to interference in the output section. Fibre-based Sagnac interferometers are commonly used for gyroscopes and have become the most commercially successful fibre sensors.

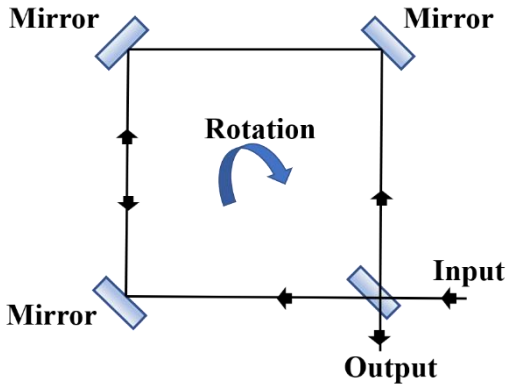

Fig. 10: Schematic diagram of Sagnac interferometer.

The Sagnac interferometer system is particularly suitable for sensing rotation. Due to the

polarisation sensitivity of fibre based Sagnac interferometers, normally polarisation maintaining fibres or polarisation controller are embedded to the system. A fibre based Sagnac interferometer sensing setup is shown in Fig. 10.

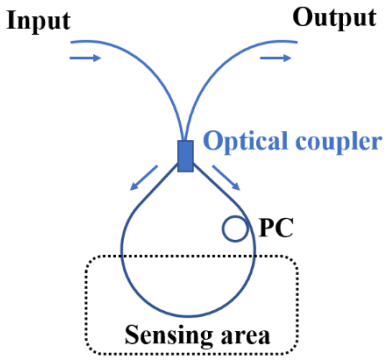

Fig. 11: A fibre based Sagnac interferometer sensing setup.

In recent years, the application of Sagnac interferometer for biochemical sensing has also drawn attention. For example, Li *et al.* [25] designed a high sensitivity biosensor with exposed core microstructured fibre. Gao *et al.* [43] achieved high sensitivity DNA detection with Sagnac interferometer based on a microfibre.

B. Fabry-Pérot interferometric sensors

The use of in-line Fabry-Pérot interferometers for fibre sensing has recently received significant attention for its relatively simple fabrication process, potentially high sensitivity and ease of multiplexing. A general Fabry-Pérot interferometer is typically formed by two weakly reflecting interfaces, such as the two mirrors and air as shown in Fig. 12. The light with incidence angle θ_i goes into the Fabry-Pérot cavity and undergoes multiple reflections and transmissions. After that, the reflected light will interfere at the incidence area. When a Fabry-Pérot interferometer is embedded into optical fibres, the incident light is perpendicular to the mirror surfaces.

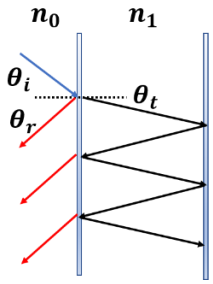

Fig. 12: Principle of Fabry-Pérot cavity.

Optical fibre Fabry-Pérot interferometers can usually be classified as two kinds, sealed cavities and open cavities. Sealed cavities are suitable to sense physical parameters like pressure, strain, temperature, and magnetic fields. Open cavities offer the opportunity to form chemical sensors and biosensors, as gases and liquids can enter the cavities directly as shown in Fig. 13. For

example, Warren-Smith *et al.* [44] applied Fabry-Pérot interferometers for bulk RI and polyelectrolyte thin film sensing with ultra-short cavities. Zhang *et al.* [45] realised thin-film and biosensing with micro-gap Fabry-Pérot interferometers.

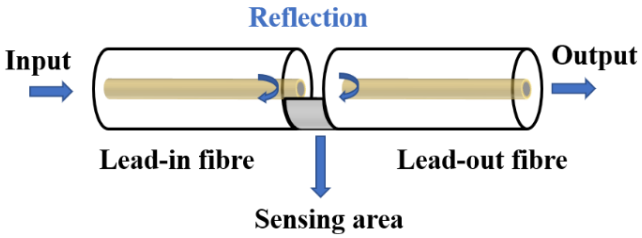

Fig. 13: An open cavity optical fibre Fabry-Pérot interferometer.

Methods for fabricating Fabry-Pérot interferometers in optical fibres have been well developed over the years. In the paper by Warren-Smith *et al.* [44], focused ion beam milling was utilised to form a cavity. Zhang *et al*. [45] used wet etching and fusion splicing instead. Many other researchers have also applied methods such as micromachining [46]. However, these methods normally involve expensive and bulky instruments or hazardous chemicals. To solve this issue, Duan *et al.* [47] fabricated a Fabry-Pérot interferometer for gap sensing by inducing a lateral offset during splicing. Accordingly, the strength of this sensor will be compromised due to relatively small splicing area. Wu *et al.* [4] proposed a method to fabricate Fabry-Pérot interferometers based on cleaving and splicing of single mode fibres and a C-shaped fibre, which is cheap and relatively straightforward.

The use of an open cavity optical fibre Fabry-Pérot interferometer fabricated by embedding a C-shaped fibre into two single mode fibres is the focus of this thesis. In particular, the ability to perform biochemical sensing with multiplexing ability using serially spliced cavities.

1.3 Laser overview

1.3.1 General laser principle

Since the first demonstration of a ruby crystal laser (or "light amplification by stimulated emission of radiation") by Miaman in 1960, the laser theory has been extended for decades by many scientists. Many kinds of lasers have been demonstrated such as solid-state lasers, gas lasers, dye lasers and semiconductor lasers. These lasers have been applied in many scientific areas besides physics due to their advantages such as coherence, high directionality and high power [48]. For example, high energy lasers can be used for particle physics, military and communication application. Some ultrashort pulsed lasers such as femtosecond lasers can be utilised for laser machining [49]. Lasers with specific wavelengths can be applied in medical areas such as skin treatment or eye surgeries [50].

Three elements are essential in laser operations: an optical gain medium, a pump source and optical feedback [48]. The gain medium provides a population of atoms or molecules that can be transferred between different energy levels so that optical gain can be obtained. It can be any state such as gas, liquid, solid or plasma. Depending on specific requirements for wavelength, many materials can be adapted as gain medium such as CO_2 (9.2–11.4 μm, 4.6–5.8 μm), He-Ne (visible to mid-infrared), neodymium-doped yttrium aluminium garnet (Nd:YAG) (ultraviolet to near-infrared with different harmonics) and some optical dyes (320-1500 nm with different dyes).

Optical pumping can transfer atoms or molecules of the gain medium from low energy levels to upper energy levels so that population inversion can be achieved, which is a fundamental process in achieving laser operation. The most commonly used pumping methods are optical pumping (by a lamp or a shorter wavelength laser) and electrical pumping (by intense electrical discharge) [48]. Electrical pumping is normally used for gas and semiconductor lasers while optical pumping is commonly used for fibre laser and many rare earth doped lasers. Based on different gain media, other pumping methods can also be utilised such as X-ray pumping, electron-beam pumping, chemical pumping and gas-dynamic pumping.

Optical feedback ensures that the generated light can be continuously amplified so that higher intensity can be obtained. Commonly used feedback is based on resonators such as Fabry-Pérot resonators or confocal resonators, which are normally formed by reflective mirrors. Recently, laser operations based on ring resonators are also significant topics.

The physical properties of lasers can be described by Maxwell's equation as discussed in the previous chapter [50]. To demonstrate the process of generating lasers, rate equations are commonly utilised. A laser is obtained by the interaction between light and matter which consists of three main processes: spontaneous emission, stimulated emission and absorption. These three processes are the basis of continuous wave laser operation. By adding in the population inversion build-up, pulsed laser operation can also be achieved.

A. Spontaneous, stimulated emission and absorption

Spontaneous emission, stimulated emission and absorption are the most important and

fundamental processes in any laser operation [51]. Assuming an ideal two-level system, each process is demonstrated in Fig. 14.

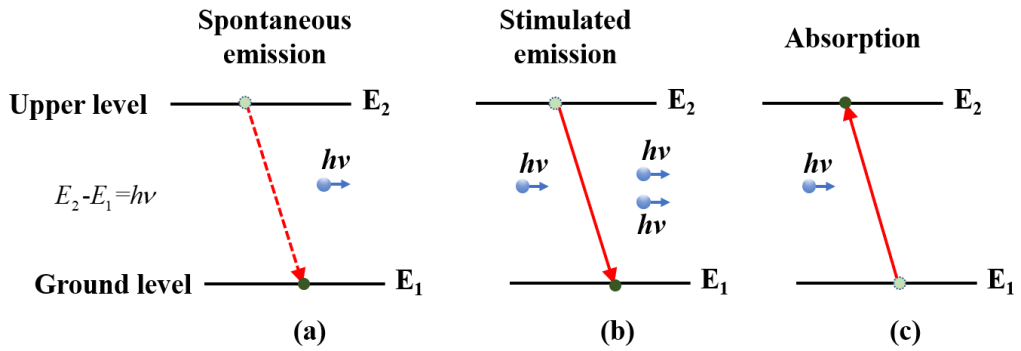

Fig. 14: (a) Spontaneous emission, (b) stimulated emission and (c) absorption.

Consider a ground energy level E_1 and upper energy level E_2 where the energy difference between them can be expressed as:

$$E_2 - E_1 = h\nu \tag{16}$$

where h is the Planck constant and ν is the photon frequency.

In Fig. 14(a), an atom or molecule resides in the upper state initially, it will decay to the ground state spontaneously according to quantum electrodynamics [50]. The energy difference will then be released by the system in the form of a photon whose frequency matches the energy difference. However, the emitted photon is in random direction and polarisation [52, 53]. Note that the spontaneous emission is a radiative process and the energy can also be released by non-radiative decay such as transferring to kinetic energy of the surrounding atoms or molecules [51, 52].

Fig. 14(b) demonstrates the stimulated emission process. When an external photon with frequency ν is injected into the gain medium, an atom or molecule in upper energy level will transfer to ground energy level while emitting another photon with the same frequency ν. The key characteristics of stimulated emission is that the emitted photon has the same polarisation, direction and phase as the incident photon in this two-level system [52]. Through this process, the incident photon is amplified to two photons. Stimulated emission is the key process for laser operation and gives the laser its coherence, unidirectionality and monochromaticity.

To ensure that the input light can be continuously amplified, continuous stimulated emission is required. As a result, getting more atoms or molecules into the upper energy level is significant for laser operations. This is achieved through absorption as demonstrated in Fig. 14(c). When a photon with frequency ν is incident on the gain medium, an atom or molecule will absorb the energy and then transfer to the corresponding upper energy level.

The rate equations used to describe these three processes can be expressed as:

$$\left[\frac{dN_2}{dt}\right]_{\substack{spontaneous\\emission}} = \frac{N_2}{\tau_{sp}} \tag{17}$$

$$\left[\frac{dN_2}{dt}\right]_{\substack{stimulated\\emission}} = W_{21}N_2 \tag{18}$$

$$\left[\frac{dN_1}{dt}\right]_{absorption} = -W_{12}N_2 \tag{19}$$

where N_2 and N_1 are the upper energy level and ground energy level population; τ_{sp} is the spontaneous emission lifetime; W_{21} and W_{12} are the stimulated emission and absorption coefficients respectively. Due to the degenerate phenomenon of real energy level system, the relationship of the stimulated emission and absorption coefficients can be obtained as:

$$g_2W_{21} = g_1W_{12} \tag{20}$$

where g_2 and g_1 are the degeneracy of the upper energy level and ground energy level respectively. Note that the stimulated emission and absorption depend not only on the populations of the energy levels but also the incident wave. The more precise expression for the stimulated emission and absorption coefficients can be obtained as:

$$W_{21} = \sigma_{21}F \tag{21}$$

$$W_{12} = \sigma_{12}F \tag{22}$$

where F is the photon flux of the incident light; σ_{21} and σ_{12} are the stimulated emission cross section and absorption cross section respectively.

To achieve a stable laser, the gain medium is required to be able to reach population inversion between the ground energy level and upper energy level which can be expressed as:

$$N_2 > \frac{g_2}{g_1}N_1 \tag{23}$$

The two-level model can be used for a general understanding of the laser operation. However, in practice it is impossible to obtain population inversion in a two-level energy system. More practical models for laser operation are four-level systems or quasi-three-level systems.

B. Continuous wave and pulsed lasers

Based on the generated laser characteristics, common lasers can be classified as continuous wave (CW) lasers and pulsed lasers.

Consider a typical four-level laser system such as CO_2 or He-Ne lasers as demonstrated in Fig.

15. The four energy levels are marked as E_0 to E_3 where the pump transfers atoms or molecules between the ground level E_0 and the upper level E_3.

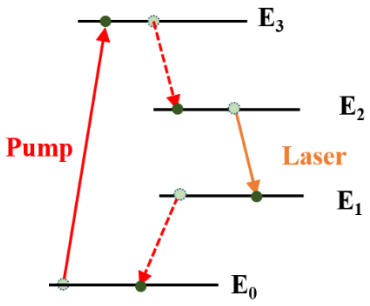

Fig. 15: A four-level laser system.

The basic laser operation is described as:

I. Initially almost all the atoms or molecules reside in ground energy level E_0.

II. The pump excites atoms or molecules from E_0 to the upper energy level E_3.

III. The atoms or molecules in E_3 will rapidly decay to E_2 due to the short lifetime. They accumulate in E_2 as that the lifetime in E_2 is much larger than E_3.

IV. The atoms or molecules will decay to E_1 through stimulated emission.

V. The atoms or molecules in E_1 will finally decay to E_0.

In this case, the population change of energy level E_2 and the total population N can be derived as:

$$\frac{dN_2}{dt} = R_p - BNN_2 - \frac{N_2}{\tau} \tag{24}$$

$$\frac{dN}{dt} = V_a BNN_2 - \frac{N}{\tau_c} \tag{25}$$

where R_p is the pumping rate; B is the stimulated transition rate per photon per mode; τ is the lifetime of upper energy level E_3; τ_c is the photon lifetime; V_a is the volume of the mode in the gain medium. The pumping rate is expressed as:

$$R_P = \frac{\eta_P P}{ALh(\nu_3 - \nu_0)} \tag{26}$$

where η_P is the pumping efficiency; P is the pumping power; A is the cross-sectional area of the pumped volume of the gain medium; L is the length of the gain medium; ν_3 and ν_0 are the frequency of the upper energy level E_3 and ground energy level E_0.

When the gain medium is continuously pumped, this laser operation can generate an output beam with relatively stable laser characteristics such as wavelength and intensity [52]. In contrast, when the pulsed pump is utilised, the laser emits light with a repetition rate R_r. The output of a CW laser and a pulsed laser are demonstrated in Fig. 16.

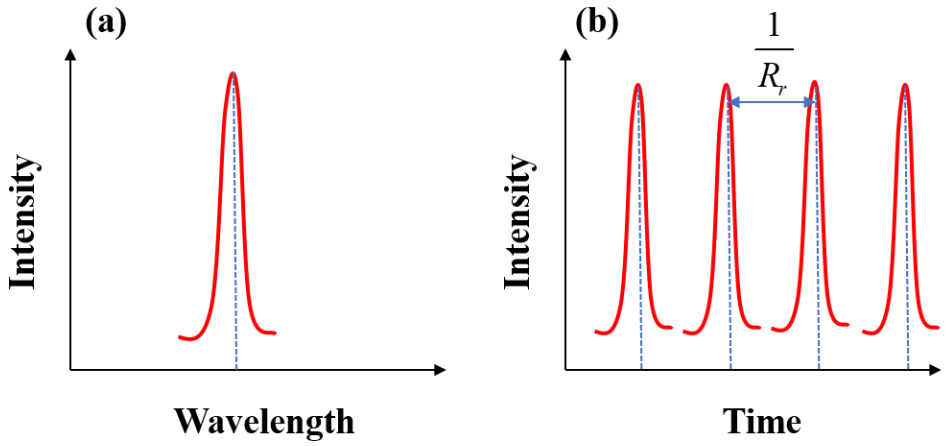

Fig. 16: (a) A CW laser and (b) a pulsed laser with a repetition rate R_r.

Other methods to obtain pulsed laser operation are based on Q-switching or mode-locking, which can be achieved by accumulating the population inversion between the upper and lower energy levels. Compared with CW laser operation, Q-switched lasers can obtain ultrashort pulses (~picosecond can be achieved) and very high peak power output.

1.3.2 Optical fibre lasers overview

Optical fibres offer a number of advantages for laser generation due to their high surface to volume ratio allowing for rapid cooling and high stability due to the avoidance of free space optical components. This allows for outcomes such as ease of configuration, high power, good beam quality, easier pulsed operation and single transverse mode operation [54-57]. Since Koester and Snitzer [53] first demonstrated that optical fibres can be utilised for infrared laser operation, many techniques such rare-earth-doped-fibre lasers, fibre dye lasers, photonic crystal fibre laser and fibre laser resonators based on fibre Bragg grating have been well developed. The wavelength coverage of fibre lasers has been expanded to mid-infrared, visible and ultraviolet spectra [58-61]. These lasers have been successfully applied into military, sensing and communications. In the following part, several typical fibre laser operations are introduced respectively.

A. Doped-fibre lasers

Doped-fibre lasers were first demonstrated at the early stage of laser development in the 1960s. Due to the limited availability of pump sources and fabrication methods, the output power of doped-fibre lasers was initially limited. Recent developments in doped-fibre lasers has led to kilowatt power scales and various options for mode, wavelength and pulse control. The principle of doped-fibre lasers is based on the light interaction with the doped rare-earth ions in the optical fibre. When light propagates inside the fibre core, the rare-earth ions will be excited to an upper energy level for lasing. The common doped fibres are regular single mode fibres with high RI core and low RI cladding geometry. For example, the first doped-fibre laser was based on neodymium (Nd^{3+})-doped core and lower RI glass cladding [53] at 1.06 μm. One

typical configuration of the doped-fibre laser is demonstrated in Fig. 17. The doped fibre is pumped continuously and the obtained laser is amplified in the cavity formed by a reflection mirror, the cleaved end of the fibre and two dichroic mirrors. The output is then monitored by an external optical spectrum analyser (OSA).

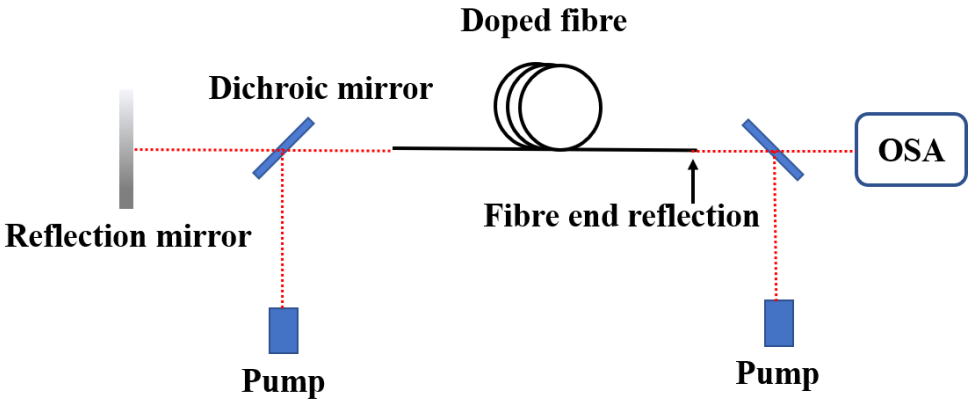

Fig. 17: Basic doped-fibre laser configuration.

Many dopants have been investigated for different wavelengths and output powers since the first doped-fibre laser demonstration. For example, Giles and Desurvire [62] modelled a fibre laser at 1.55 µm wavelength by doping erbium (Er^{3+}) with a 1.48 µm pump. Dianov *et al.* [63] introduced a bismuth doped-fibre laser. To obtain higher power lasers, some techniques such as double-clad optical fibres are also utilised. For instance, Jeong *et al.* [64] achieved a CW ytterbium-doped laser with an output as high as 1.36 kW through a double-clad large core fibre. This fibre increases the output power whilst decreasing the numerical aperture (NA) so that the beam quality is improved. Solodyankin *et al.* [65] developed a 1.93 µm fibre laser by doping thulium (Tm). A carbon nanotube absorber was utilised to obtain mode locking in this project. To obtain broadband lasers, many researchers doped the fibres with two or more dopants [66]. For example, the Nd: YAG fibre laser can provide different wavelength lasing through the generation of different harmonics. Many fabrication methods for doped laser has been introduced. Normally a doped-fibre laser is fabricated by chemical-vapour-deposition and solution doping during preform fabrication [64].

B. Optical fibre dye lasers

A fibre dye laser is normally based on organic dyes with complex energy levels. Compared with traditional four-level laser or quasi-three-level gain media, organic dyes normally consist of singlet states and lower energy triplet states, shown in Fig. 18.

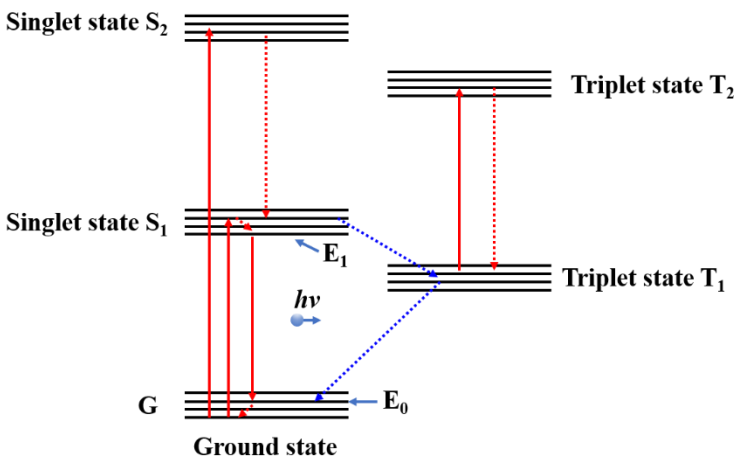

Fig. 18: Typical organic dye energy level structure.

To obtain laser operation, an external pump first excites the dye molecules to higher energy levels of the singlet state S_2. The molecules will then non-radiatively decay to the lowest energy level of S_1 which is referred as E_1. The laser operation occurs between E_1 and a high energy level (E_0) of the ground state G. However, it is possible that the molecules can also decay to the metastable triplet state T_1, which is known as intersystem crossing. The triplet states play a significant role in dye laser operation as the intersystem crossing can strongly influence the stimulated emission process of dye molecules in two ways [67]. First, the intersystem crossing decreases the population density of the upper energy level E_1 which makes the population inversion more difficult. Second, the triplet absorption between the two triplet states induces more loss to the laser oscillation due to that the energy difference between these triplet states is close to the according singlet states energy difference. The solution to these problems is to establish the population inversion between the ground state and upper state fast enough before the molecules accumulate in the triplet states. In practice, pulsed laser pumping is utilised to provide the fast population inversion.

The use of dye as a gain medium for lasing was first introduced in 1964 by Stockman *et al.* [68]. The authors indicated that a dye laser based on organic molecules can provide high power output with wavelength tunability. After that, many efforts have been made to develop optical fibre dye lasers due to their advantages such as small size and high energy density. Pendock *et al.* [69] demonstrated a dye laser based on a tapered single mode fibre with a 2 μm waist diameter. The fibre taper is surrounded by Rhodamine 6G and the evanescence wave facilitates the optical pumping. Gerosa *et al.* [70] developed a microfluidic laser operation with a Fabry-Pérot cavity formed by two air gaps. Similarly, Zhou *et al.* [71] reported a microcavity dye laser that utilised gold films on the fibre ends to provide reflections. Microstructured optical fibres can also be used for fibre dye laser operation. For instance, Li *et al.* [72] developed a micro-ring laser by implementing a hollow-core microstructured optical fibre. Many kinds of dye are explored to provide laser operation and coverage of wavelength has been widely expanded (320-1500 nm).

In this thesis, optical fibre dye lasers are discussed using microcavities fabricated with C-shaped fibre and exposed core fibre. These configurations allow very small volumes to be used and allow for microfluidics to be implemented with rapid dye circulation. This area of research can

also be expanded in future to allow for more exotic gain materials to be used, such as quantum dots or rare earth doped nanoparticles.

Chapter 2 Optical fibre sensing with C-shaped fibres

2.1 Introduction

In this chapter, optical fibre sensors with multiplexing ability are proposed based on Fabry-Pérot interferometers formed by splicing C-shaped fibre between single mode fibres. Sensors formed by one C-shaped fibre cavity and dual C-shaped fibre cavities are discussed individually. Refractive index is the most widely used measurand for sensing, so it is first demonstrated using a single cavity by filling and measuring NaCl solutions with different concentrations. The multiplexing ability is then examined by filling different NaCl solutions into the dual cavity system. The results show minimal crosstalk between the two interferometers. The dual-cavity interferometric sensor is then applied to biochemical sensing by utilising polyelectrolyte layer-by-layer self-assembly followed by the biotin functionalisation and streptavidin sensing process. The proposed sensors can provide high sensitivity for RI sensing and it solves an important problem in biochemical sensing by providing an ability to simultaneously measure a negative control, critical for reducing false positive measurements.

2.2 Theory

In this project, the optical fibre sensors are considered to be Fabry-Pérot interferometers with weakly reflecting mirrors. To estimate the power loss induced by the C-shaped fibre as well as characterising the effect from measurand change, the single interferometers and dual interferometers were explored respectively. For single interferometers, the visibility and interference spectra were simulated with regards to length. For the dual interferometers, the modulation and demodulation of multiple reflections were studied with a phase-demodulation technique based on fast Fourier transform (FFT). In the end, the effect from thin film coating process was estimated by transfer matrix method (TMM).

2.2.1 Single cavity interferometer

A single interferometer is constructed by splicing a short piece of C-shaped fibre between two single mode fibres (SMF). This forms a Fabry-Pérot interferometer with the SMF-C-SMF structure as shown in Fig. 19.

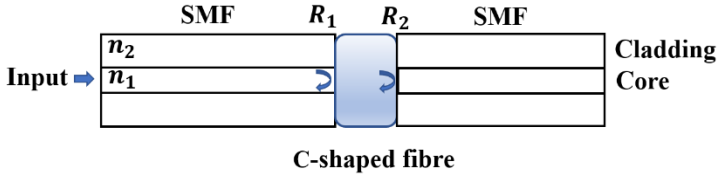

Fig. 19: C-shaped fibre Fabry-Pérot interferometer.

For the C-shaped interferometers, the two interfaces between SMF and C-shaped fibre function

as two weakly reflecting mirrors that create a two-wave interferometer. To explore the transmission and reflection of the cavities, it can be assumed that both incidence to the two mirrors are normal. In fact, the assumption is acceptable as the length of the cavity is normally comparable to the Rayleigh length, which is:

$$Z_R = \frac{\pi\omega_0^2}{\lambda} \tag{27}$$

where ω_0 and λ are the spot size and wavelengrh of the light inside the interferometer respectively.

From the Fresnel equation, the reflectivity of the two interfaces are characterised by the RI of fibre core n_1 and air n_0:

$$R_1 = R_2 = \left|\frac{n_1 - n_0}{n_1 + n_0}\right|^2 \tag{28}$$

The mode radius ω of a propagating light at wavelength λ inside an optical fibre can be expressed as [2]:

$$\omega = a \cdot (0.65 + \frac{1.619}{V^{1.5}} + \frac{2.879}{V^6}) \tag{29}$$

where V is recognised as V parameter and it characterises the RI contrast between the fibre core and cladding; a is the radius of the fibre core:

$$V = \frac{2\pi a}{\lambda}\sqrt{n_1^2 - n_2^2} \tag{30}$$

The beam is then diverging as it propagates and the beam waist at a distance z changes according to:

$$\omega^2(z) = \omega_0^2 \cdot [1 + (\frac{\lambda \cdot z}{\pi n_m \omega_0^2})^2] \tag{31}$$

where $\omega(z)$ is the beam radius at a distance z from the waist position; n_m is the RI of the medium; ω_0 is the spot size of the light.

When the propagating beam couples into another fibre, the difference of beam waist induces a coupling loss, which is related to the mode field diameter mismatch between the fibres and the expanded beam. The coupling efficiency from a fibre with beam radius ω_1 to another fibre with beam radius ω_2 can be expressed as:

$$\eta = \frac{4\omega_1^2\omega_2^2}{(\omega_1^2+\omega_2^2)^2} \tag{32}$$

In this case, ω_1 is the beam radius at the interface I and ω_2 is the beam radius at the interface I after diverging inside the interferoeter for a roundtrip and ω_0 is the beam radius within the SMF core as shown in Fig. 20.

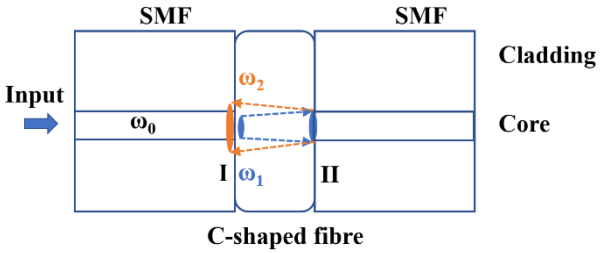

Fig. 20: Beam radius divergence inside singe cavity interferometer.

Consider a C-shaped fibre with length L, the beam radius can be calculated as:

$$\omega_2^2 = \omega^2(L) = \omega_0^2 \cdot [1+(\frac{\lambda_0 \cdot 2L}{\pi n_m \omega_0^2})^2] \tag{33}$$

$$\omega_1 = \omega_0 \tag{34}$$

The Fabry-Pérot interferometers can be treated as a two-beam interferometer due to the weak reflection on each interface (3.3% at 1550 nm), the interference spectrum can be expressed with the two reflections:

$$I(\lambda) = I_1 + I_2 + 2\sqrt{I_1 I_2}\cos(\frac{4\pi n_m L}{\lambda} + \varphi_0) \tag{35}$$

I_1 and I_2 are the intensity of the reflections from two mirrors, respectively; n_m is the RI of medium filling inside the interferometer; φ_0 is the initial phase difference between I_1 and I_2, it is set as 0 for simplification.

From the theory of Fresnel reflection, the intensity on each interface can be expressed with the input intensity I_0, the reflectivity R_1, R_2, the transmissivity at the first interface T_1 and coupling efficiency η as:

$$I_1 = I_0 R_1 \tag{36}$$

$$I_2 = I_0 T_1^2 R_2 \eta \tag{37}$$

When considering the effect of the cavity length, the interference visibility V_i is a key parameter:

$$V_i = \frac{2\sqrt{I_1 I_2}}{I_1 + I_2} \tag{38}$$

Simulations have been conducted with the SMF-28, which is standard single mode fibre with core RI n_1=1.4439 at wavelength of 1550 nm and core radius a=4.1 μm. This interferometer is filled with water, whose RI is approximately 1.330.

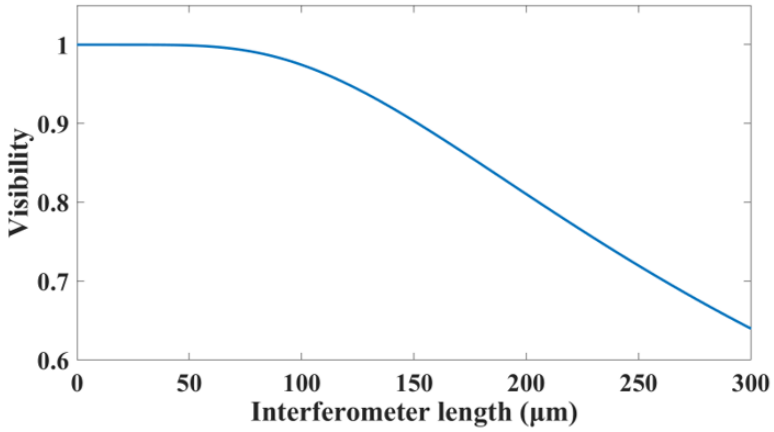

Fig. 21: Visibility for interferometers.

As demonstrated in Fig. 21, when the length of interferometer increases, the visibility will decrease accordingly. During the experiments, the length needs to be properly controlled to obtain sufficient visibility. When the length of the cavity is zero, the visibility should be 1 due to the absence of divergence. But in fact, the length of the cavity cannot be too short or the free spectral range (FSR) may be difficult to detect and also there is always a limitation for the fabrication.

From the interference spectra as shown in Fig. 22, the analysis about the visibility is more obvious. When the length of cavity is longer, there will be more fringes on the spectra, and the visibility will be smaller.

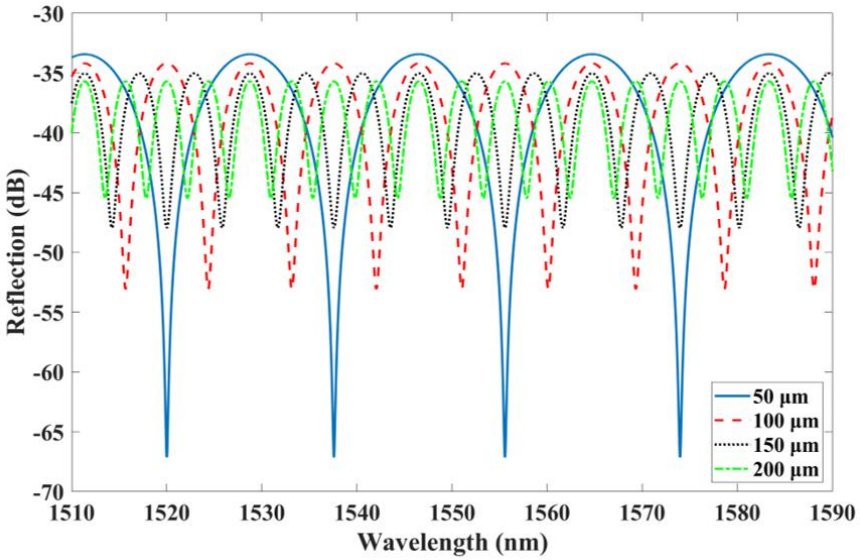

Fig. 22: Simulation of reflection of the single cavity with different length using the analysis above, (a) L=30 µm, (b) L=50 µm (c) L=100 µm and (d) L=150 µm.

2.2.2 Dual cavity interferometer

A dual interferometer is fabricated by combining two SMF-C-SMF structures as shown in Fig. 23.

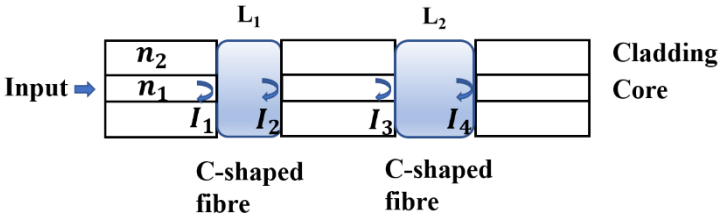

Fig. 23: Dual Fabry-Pérot interferometer.

For the dual cavity, there are four individual reflections from each interface between single mode fibres and C-shaped fibres. The interference spectrum is then modulated by each reflection, which can be expressed as:

$$I(\lambda)=\{I_1+I_2+2\sqrt{I_1I_2}\cos(\frac{4\pi n_{m1}L_1}{\lambda})\}+\{I_1+I_3+2\sqrt{I_1I_3}\cos[\frac{4\pi(n_{m1}L_1+n_1L)}{\lambda}]\}$$
$$+\{I_1+I_4+2\sqrt{I_1I_4}\cos[\frac{4\pi(n_{m1}L_1+n_1L+n_{m2}L_2)}{\lambda}]\}+\{I_2+I_3+2\sqrt{I_2I_3}\cos(\frac{4\pi n_1L}{\lambda})\} \quad (39)$$
$$+\{I_2+I_4+2\sqrt{I_2I_4}\cos[\frac{4\pi(n_{m2}L_2+n_1L)}{\lambda}]\}+\{I_3+I_4+2\sqrt{I_3I_4}\cos(\frac{4\pi n_{m2}L_2}{\lambda})\}$$

where $I(\lambda)$ is the optical intensity of the overall interference spectrum; I_1 to I_4 are reflections from four interfaces; n_{m1}, L_1 and n_{m2}, L_2 are RI of the medium and length of the two interferometers; n_1 is RI of the core of the single mode fibre; λ is free space wavelength of the propagating light. This interference spectrum is formed by the six possible combinations of the four reflections.

Each intensity in this equation is given by:

$$I_1 = I_0 R_1 \tag{40}$$

$$I_2 = I_0 R_1 T_1 \eta_{12} T_1 \tag{41}$$

$$I_3 = I_0 T_1 T_1 \eta_{11} R_2 T_1 \eta_{11} T_1 \tag{42}$$

$$I_4 = I_0 T_1 T_1 \eta_{11} T_2 R_2 T_2 \eta_{22} T_1 T_1 \eta_{12} \tag{43}$$

where R_1 and T_1 are the reflectance and transmittance of the first interferometer; R_2 and T_2 are the reflectance and transmittance of the second interferometer individually; η_{11}, η_{12} and η_{22} are the coupling efficiency on the surfaces respectively. Each parameter mentioned above are given by:

$$R_1 = (\frac{n_1 - n_{m1}}{n_1 + n_{m1}})^2 \tag{44}$$

$$T_1 = 1 - R_1 \tag{45}$$

$$R_2 = (\frac{n_2 - n_{m2}}{n_2 + n_{m2}})^2 \tag{46}$$

$$T_2 = 1 - R_2 \tag{47}$$

$$\eta_{11} = \frac{4\omega_0^2 \omega_1^2}{(\omega_0^2 + \omega_1^2)^2} \tag{48}$$

$$\eta_{12} = \frac{4\omega_0^2 \omega_2^2}{(\omega_0^2 + \omega_2^2)^2} \tag{49}$$

$$\eta_{22} = \frac{4\omega_0^2 \omega_3^2}{(\omega_0^2 + \omega_3^2)^2} \tag{50}$$

The coupling efficiency is related to beam waist and ω_0 is the spot size of beam inside the single mode fibre; ω_1 and ω_2 are the beam waist of beams propagating distance L_1 and $2L_1$ where L_1 is the length of the first interferometer; ω_3 is the beam waist of beams propagating distance $2L_2$ which is the length of the second interferometer. They are shown in and can be expressed as:

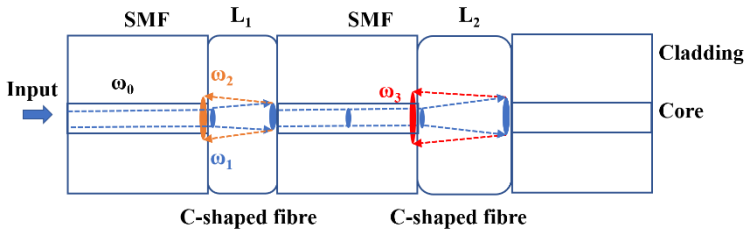

Fig. 24: Beam radius divergence inside dual cavity interferometers.

$$\omega_1 = \omega_0 \sqrt{1+(\frac{\lambda \cdot L_1}{\pi n_{m1} \omega_0^2})^2} \tag{51}$$

$$\omega_2 = \omega_0 \sqrt{1+[\frac{\lambda \cdot (2L_1)}{\pi n_{m1} \omega_0^2}]^2} \tag{52}$$

$$\omega_3 = \omega_0 \sqrt{1+[\frac{\lambda \cdot (2L_2)}{\pi n_{m2} \omega_0^2}]^2} \tag{53}$$

where n_{m1} and n_{m2} are the RI of the medium inside the first and second interferometer respectively.

While the reflection spectrum is complex due to multiple reflections from the two interferometers, individual interferences corresponding to each interferometer can be obtained by applying FFT on the reflection spectrum. Each peak in the FFT spectrum corresponds to an individual interference (a cosine term) and therefore can be separated and its phase change can be independently tracked. Fig. 25 demonstrates the reflection from a dual interferometer formed by 80 μm and 183 μm cavities.

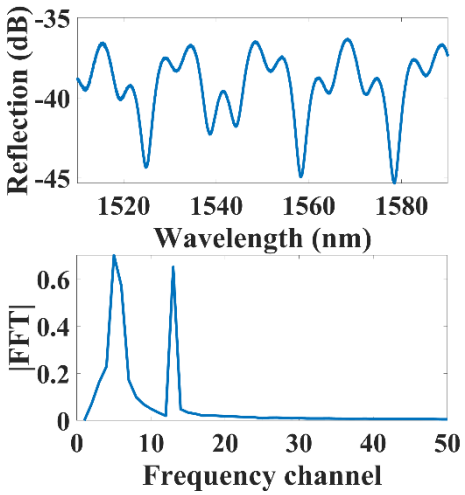

Fig. 25: (a) Reflection spectrum of the dual interferometer and (b) its fast Fourier transform spectrum (80 μm interferometer plus 183 μm interferometer).

2.2.3 Phase-demodulation

In this project, sensing is realized by monitoring the phase change induced by the measurand

change through a phase-demodulation technique. When the optical path length inside the cavity changes, such as due to RI or applied thin films, the interferometer reflection spectrum will experience a phase shift. This phase shift can be demodulated by extracting the Fourier phase change at the corresponding Fourier frequency. Using the single interferometer as an example, the interference spectrum (35) can be first rewritten as (56) where d is the optical path length of the interferometer. By introducing an optical path disturbance Δd, the FFT of the spectrum becomes (58). The disturbance applied on the optical path can then be transferred to the change in wavelength [73] as in (56). Within a narrow wavelength domain, the wavelength can be replaced by central wavelength λ_0.

$$I(\lambda) = I_1 + I_2 + 2\sqrt{I_1 I_2}\cos(\frac{2\pi}{\lambda}\cdot d) \tag{54}$$

$$I'(\lambda) = I_1 + I_2 + 2\sqrt{I_1 I_2}\cos[\frac{2\pi}{\lambda}\cdot(d-\Delta d)] \tag{55}$$

$$\Delta\lambda = \frac{\lambda\cdot\Delta d}{d-\Delta d} \approx \frac{\lambda_0\cdot\Delta d}{d-\Delta d} \tag{56}$$

The FFT of the undisturbed spectrum, F(f_k), and the disturbed spectrum, F'(f_k), are then obtained as:

$$F(f_k) = \sum_{j=1}^{N} I(\lambda_j)\cdot\cos[\frac{2\pi}{N}\cdot(j-1)(k-1)] - i\sum_{j=1}^{N} I(\lambda_j)\cdot\sin[\frac{2\pi}{N}\cdot(j-1)(k-1)] \tag{57}$$

$$F'(f_k) = \sum_{j=1}^{N} I'(\lambda_j)\cdot\cos[\frac{2\pi}{N}\cdot(j-1)(k-1)] - i\sum_{j=1}^{N} I'(\lambda_j)\cdot\sin[\frac{2\pi}{N}\cdot(j-1)(k-1)] \tag{58}$$

$$\lambda_j = \lambda_1 + (\mathrm{j}-1)\cdot\Delta\lambda_0 \tag{59}$$

$$f_k = \frac{k-1}{N\cdot\Delta\lambda_0} \tag{60}$$

where λ_j is the sampling wavelength and f_k is the intrinsic spatial frequency. The phase shift of the spectrum $\Delta\varphi$ can then be expressed as:

$$\Delta\varphi = \tan^{-1}\left\{\frac{\mathrm{Im}[F'(f_k)]}{\mathrm{Re}[F'(f_k)]} - \frac{\mathrm{Im}[F(f_k)]}{\mathrm{Re}[F(f_k)]} \Big/ 1 + \frac{\mathrm{Im}[F(f_k)]}{\mathrm{Re}[F(f_k)]}\cdot\frac{\mathrm{Im}[F'(f_k)]}{\mathrm{Re}[F'(f_k)]}\right\} \tag{61}$$

where *Im* and *Re* stand for the imaginary and real part of the FFT results.

In practice, the process of obtaining the phase shift can be described as in Fig. 26. Consider that

the interference spectrum according to (35) has a sinusoidal (or equally cosine) function *y=sin(x)* and a small change in the optical path length is approximately represented as a phase shift δ applied as shown in Fig. 26(a) and Fig. 26(c). The corresponding FFT spectrum is shown in Fig. 26(b) and Fig. 26(d), where the absolute value of the FFT does not change, but the complex phase value changes by δ. In this project, the phase value was extracted at the peak of |FFT|, which represents the shift of the interference spectra.

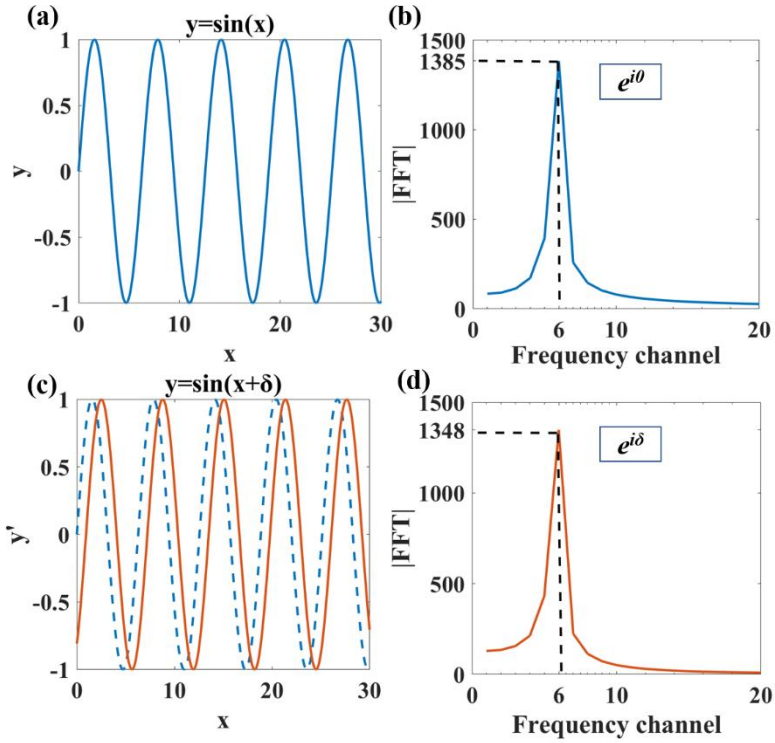

Fig. 26: Phase demodulation process. (a) Spectrum of y=sin(x) and (c) spectrum of y'=sin(x+δ) and their FFT spectra (b) and (d).

2.2.4 Transfer matrix method for thin film analysis

For RI sensing there is a clear relationship between the phase shift and any RI change, given by the argument of the cosine functions in (35) and (41). This is not as straightforward in the case of biochemical sensing, which is achieved via the deposition of thin films, where there are two competing effects: (I) Thin films effectively decrease the physical length of the interferometer, but, (II) increase the RI (the RI of any biochemical coating is typically larger than silica). The former decreases the optical path length, while the later increases it. To predict the phase change during the coating process for a single interferometer and to check that these competing processes do not cancel each other out, a simple one-layer coating model was simulated by applying the transfer matrix method (TMM) as shown in Fig. 27.

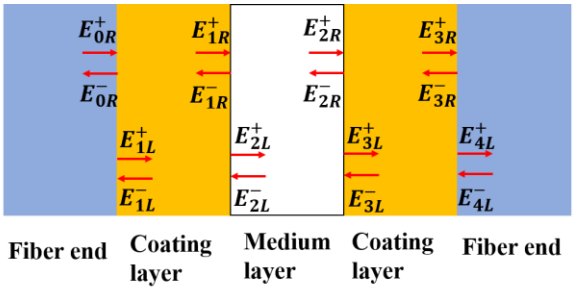

Fig. 27: One-layer coating simulation model for a single interferometer using the TMM. Red arrows indicate the direction of propagation.

Fig. 27 shows the electric field distribution in this one-layer coated system. There are two counterpropagating electromagnetic (EM) waves on each interface. The overall EM field on each interface can be expressed in vector form:

$$E_{iR} = \begin{bmatrix} E_{iR}^{+} \cdot e^{-ik_i x} \\ E_{iR}^{-} \cdot e^{ik_i x} \end{bmatrix} \tag{62}$$

$$E_{iL} = \begin{bmatrix} E_{iL}^{+} \cdot e^{-ik_i x} \\ E_{iL}^{-} \cdot e^{ik_i x} \end{bmatrix} \tag{63}$$

where E_{iR} and E_{iL} are the fields on the right and left side of the i^{th} layer; k_i is the propagation constant of the i^{th} layer and the + superscript and – superscript indicating the fields propagating towards right and left, respectively. The propagation in the medium and transmission on the interfaces are characterized by P and M matrix, respectively.

According to transfer matrix method, the field distribution can be expressed by the former field [74], such as:

$$E_{4L} = (M_{34}P_3M_{23}P_2M_{12}P_1M_{01}) \cdot E_{0R} = M_0 \cdot E_{0R} \tag{64}$$

$$M_{ij} = \frac{1}{t_{ij}} \begin{bmatrix} r_{ij} & 1 \\ 1 & r_{ij} \end{bmatrix} \qquad r_{ij} = \left| \frac{n_j - n_i}{n_j + n_i} \right| \qquad t_{ij} = 1 - r_{ij} \tag{65}$$

where M_{ij} is the transmission matrix from layer i to layer j; r_{ij} is the reflection coefficient on interface between layer i and layer j; t_{ij} is the transmission coefficient on interface between layer i and layer j; n_i is the RI of each layer. The transmission matrix P in each layer can be expressed as:

$$P_i = \begin{bmatrix} 0 & e^{-ik_i d_i} \\ e^{ik_i d_i} & 0 \end{bmatrix} \qquad k_i = \frac{2\pi}{\lambda_i} \tag{66}$$

where k_i is the propagation constant in each layer.

The field distribution in the left side of layer 4 can be written in detail as:

$$E_{4L} = \begin{bmatrix} E_{4L}^{+} \\ E_{4L}^{-} \end{bmatrix} = M_0 \cdot \begin{bmatrix} E_{0R}^{+} \\ E_{0R}^{-} \end{bmatrix} = \begin{bmatrix} M_0(00) & M_0(01) \\ M_0(10) & M_0(11) \end{bmatrix} \cdot \begin{bmatrix} E_{0R}^{+} \\ E_{0R}^{-} \end{bmatrix} \tag{67}$$

Because that there is no light entering the system from the right side, so:

$$E_{4L}^{-} = 0 \tag{68}$$

Then the field distribution of each layer can be expressed with the last layer's distribution as:

$$E_{iR}^{+} = -\frac{M_0(ji)}{M_0(ji)} \cdot E_{iR}^{-} \tag{69}$$

$$E_{iR}^{-} = 1/\left[\frac{M_i(jj) \cdot M_i(ii)}{M_i(ji)} + M_i(ij) \right] \cdot E_{4L}^{+} \tag{70}$$

For each layer:

$$M_1 = M_{34} P_3 M_{23} P_2 M_{12} \tag{71}$$

$$M_2 = M_{34} P_3 M_{23} \tag{72}$$

$$M_3 = M_{34} \tag{73}$$

By applying the TMM, we can analyze the multiple reflections and transmission for the whole system as they are expressed in terms of the overall EM fields for each layer. The simulation results in Fig. 28 shows the impact for both processes discussed before. The trend in Fig. 28(a) shows that when the coating thickness is increased, the overall phase of the interferometers decreases, which reveals that the process (I) (thin films decrease the physical length of the interferometer) is the dominant effect for the interferometer. Fig. 28(a) also reveals that the sensors are expected to be more sensitive to lower RI coatings. This is again highlighted in Fig. 28(b), which demonstrates that as the coating RI is increased the added optical path length through the coating counters the sensitivity due to decreased physical path length (reflection from the liquid-coating interface), resulting in a slight decrease in sensitivity.

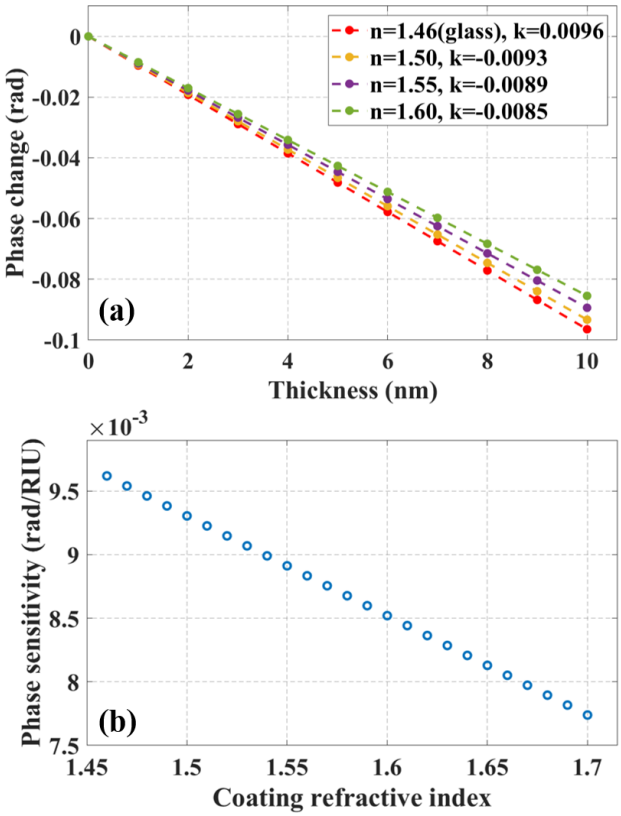

Fig. 28: Transfer matrix method simulation for a 150 µm long thin film coated single interferometer. (a) Calculated phase change for different coating thicknesses and refractive indices and (b) phase sensitivity for different coating refractive indices.

2.3 Sensor fabrication

The fabrication of the sensor was based on serially splicing C-shaped fibre between SMF. C-shaped fibre was fabricated in-house with an inner bore diameter of 40 µm and an outer diameter of 160 µm. A cross-sectional image is shown in Fig. 29(a). To fabricate an in-line interferometer, a single mode fibre and a C-shaped fibre were first cleaved with a flat end. The SMF and the C-shaped fibre were then spliced together as shown in Fig. 29(b). The C-shaped fibre was then cleaved to the desired length [Fig. 29(c)] and spliced to a second single mode fibre [Fig. 29(d)]. Multiplexed sensors can then be fabricated by serially connecting subsequent C-shaped fibre interferometers. After the fabrication of the sensors, the interferometers were enclosed in a glass capillary (inner diameter 650 µm) with inlet and outlet for future experiments as shown in Fig. 30.

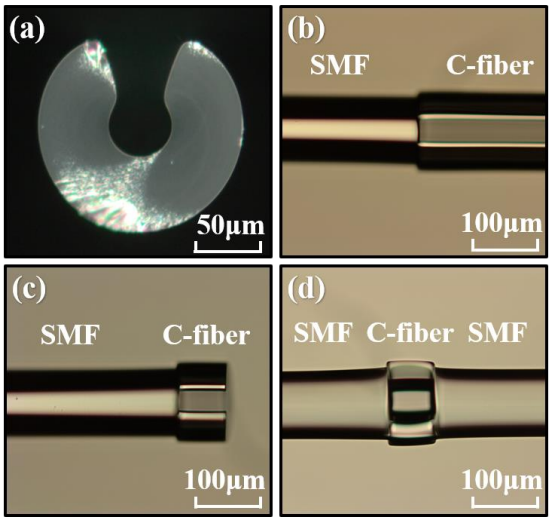

Fig. 29: (a) Cross-section of a C-shaped fibre; (b) SMF spliced with a C-shaped fibre; (c) C-shaped fibre cleaved with controlled length; (d) splice with a second SMF.

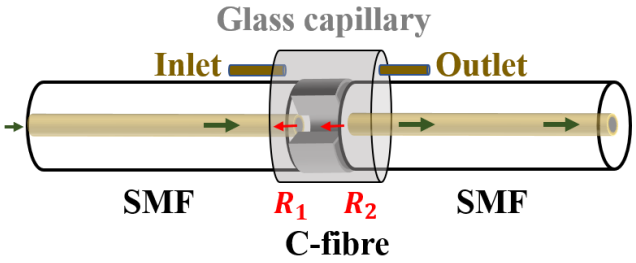

Fig. 30: Enclosed fibre sensor.

2.3.1 Cleaving

Cleaving is the process to break a fibre with a flat end prepared for future splicing. The quality of cleaving is significant to reduce the coupling loss. The most utilised strategy for cleaving is scribe and tension strategy. That is, during the cleaving process, the blade of the cleaver will make a small crack at the edge of the fibres and then the crack will extend to the whole cleaving surface with a flat end by applying longitudinal tension as shown in Fig. 31.

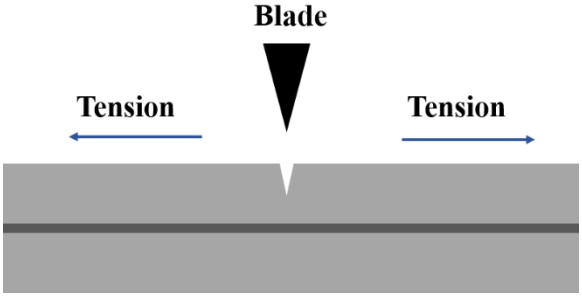

Fig. 31: Principle of fibre cleaving.

Due to the relatively strong structure of SMF, the cleaving process for SMFs is relatively easy to control. However, the C-shaped fibre is very fragile so that bad cleaving tension will lead to

large cleaving angle, which induces large scattering loss as demonstrated in Fig. 32. Bad cleaving can also lead to significant deformation during fusion, which may block the C-shaped cavities. In this project, a Fujikura CT-32 and York FK11 cleaver were used for SMF and C-shaped fibre respectively [Fig. 33].

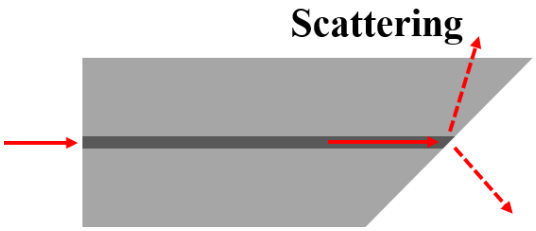

Fig. 32: Scattering loss due to angled cleaving.

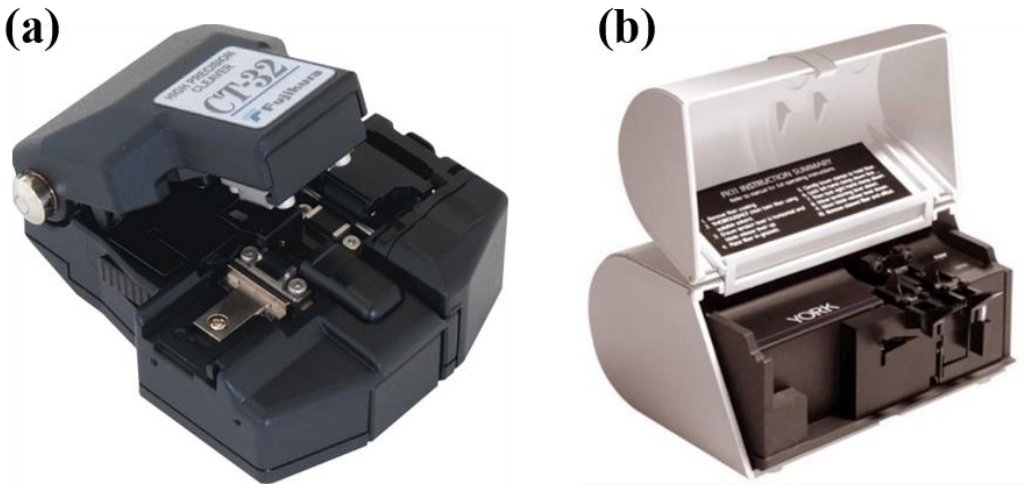

Fig. 33: (a) Fujikura (CT-32) and (b) York (FK-11) cleavers.

For cleaving C-shaped fibres, the position of the open side of the C-shaped fibre has critical impact on the cleaving quality. In most cases, bad position may only lead to a large cleaving angle, but the fibres may be broken during the fabrication if the open side is facing the blade. In this project, the open side is adjusted by observing the C-shaped fibre open side under a microscope first to ensure it is facing up (perpendicular to the blade). The impact of cleave tension is shown in Table 1.

Table 1: Performance of cleaving angle with different tension

	1	*2*	*3*	*4*	*5*	*6*	*7*	*8*	*9*
Tension	190g	180g	180g	170g	170g	170g	160g	160g	160g
Cleaving angle	18.4	7.6	0.8	0.6	0.2	0.5	0.4	0.8	0.7

Table 1 demonstrates that a tension between 160-170g produces smaller cleaving angles. In this

project, the cleaving tension of the C-shaped fibre was set to 160g.

2.3.2 Splicing

The splicing used in this project is based on fusion splicing. A Fujikura splicer (FSM-100P) was used for the splicing. The settings of the splicer have great impact on the splicing strength. Two key parameters for splicing are arc current and arc time. These two parameters were explored as demonstrated in Table 2.

Table 2: Results in terms of different arc current and arc time

	Arc current(mA)	*Arc time(ms)*	*Tension(g)*	*Results*
1	STD-4.0	3500	220	Broken splicing point
2	STD-4.0	3500	170	Broken splicing point
3	STD-3.0	3500	170	Broken splicing point
4	STD-2.5	3500	170	Broken splicing point
5	STD-2.5	3500	180	Broken splicing point
6	STD-2.5	3500	160	Broken splicing point
7	STD-2.0	3500	160	Well spliced
8	STD-2.0	3500	165	Well spliced
9	STD-2.0	3500	170	Well spliced

The standard (STD) current is a calibrated reference value for the splicer, which was 15.8 mA during this project. From Table 2, tests 1-6 show that small arc current and high tension make the splicing point easy to be broken during the second cleaving. Test 7-9 show that the splicer settings with arc current of STD-2.0mA and arc duration of 3500 ms form a sufficiently strong splice such that it can be handled in the subsequent experiments.

2.4 Experimental method

2.4.1 Temperature sensing

The proposed sensors can be potentially used for temperature sensing. The water-based analyte solutions have high thermo-optic effect and the silica fibres will also undergo thermal expansion

due to any temperature changes. In addition, biochemical sensing typically requires multiple steps including incubation periods for surface binding and the experiment duration time can be the order of hours. Therefore, the temperature sensitivity needs to be characterised before the biochemical sensing experiments.

Fig. 34: In Vitro Technologies WNB 7 waterbath.

To explore the effect from temperature, a waterbath (In vitro technologies, WNB 7) with stable controlled temperature was utilised to change the ambient temperature as shown in Fig. 34. The sensors were first put into the waterbath with a fixed temperature to characterise the temperature stability. Then the temperature was changed from 25℃ to 60℃ to quantify the temperature sensitivity. The setup used is shown in Fig. 35. An optical sensor interrogator (National Instruments, PXIe-4844), with swept output wavelength from 1510 nm to 1590 nm, was utilized to measure the reflection spectra of the sensors. The sensors were connected to a peristaltic pump to facilitate the flowing of the solutions.

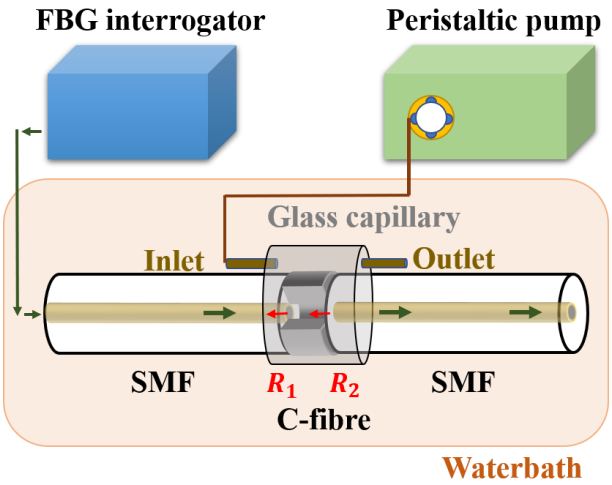

Fig. 35: The experimental setup for temperature sensing.

2.4.2 Refractive index sensing and biosensing

Similar experimental setups were utilised for RI sensing and biosensing as shown in Fig. 35. In the sensing experiments, the waterbath was used to provide a stable temperature environment. Note that in multiplexed refractive index sensing and biosensing experiments, a dual cavity system was utilised where both the interferometers were placed into the waterbath as demonstrated in Fig. 36.

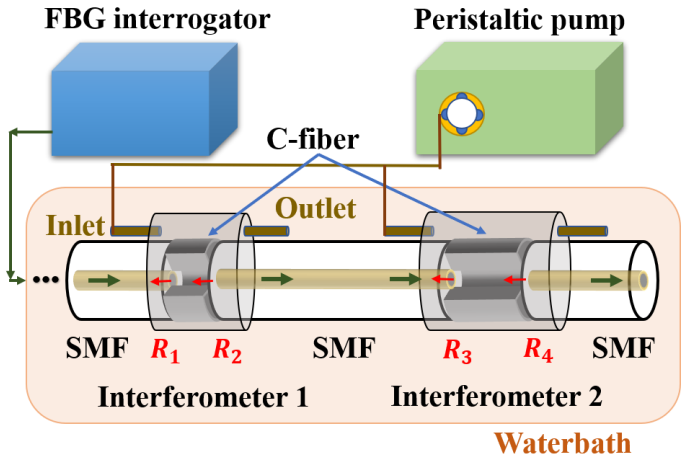

Fig. 36: Experimental setup for multiplexed RI sensing and biosensing.

A. RI sensing and multiplexing ability verification

The setup used for RI sensing is demonstrated in Fig. 36. Analyte solutions of varying RI were prepared via serial dilution of NaCl in distilled water with small and large concentration intervals. One set ranged from 0.1% to 1.0% (n = 1.3341 to n = 1.3357) in steps of 0.1% while the other ranged from 1% to 10% (n =1.3362 to n = 1.3515) in steps of 1%. The RI sensing was demonstrated on a single interferometer system by circulating different NaCl solutions into the interferometer while monitoring the real-time phase change simultaneously.

The multiplexing ability of the sensors were tested by measuring the crosstalk between the two interferometers. This was performed by filling the series of sodium chloride (NaCl) solutions into one of the interferometers with water as a reference in the alternate interferometer.

B. Multiplexed biosensing

To demonstrate multiplexed biochemical fibre sensing, a dual interferometer system was utilised where both interferometers were first coated with three polyelectrolyte layers, as indicated in Fig. 37. Polyelectrolytes are small charged polymers that can bind to surfaces such as glass through electrostatic interactions and can be used to create a surface with specific chemical functional groups for further biochemical attachment. First, the interferometers were rinsed with water and boiled for three hours to remove any contaminants. A PAH (poly-allylamine hydrochloride, 2 mg/mL in 1 M NaCl) polyelectrolyte solution was then pumped into the interferometers to deposit the first layer. The interferometers were then rinsed with 1 M NaCl solution to remove any unbound PAH molecules. Secondly, a PSS (poly-sodium 4-styrene sulfonate, 2 mg/mL in 1 M NaCl) polyelectrolyte solution was pumped into the

interferometers to deposit the second layer. Finally, a PAH coating was applied again to complete the three-layer structure. The number of layers can be altered but the sensors should be terminated with PAH to provide the amine functional groups that are required to bind the subsequent biotin layer.

Following the polyelectrolyte coating process, one cavity was monitored as a negative control with PBS (phosphate-buffered saline, 2 mg/mL in 1 M NaCl) solution while the other was coated with biotin (EZ-Link Sulfo-NHS-LC-biotin, 0.2 mg/mL). Subsequently the target protein, streptavidin (Invitrogen, 0.5 mg/mL in PBS), was pumped into both interferometers. As streptavidin has strong binding affinity to biotin, but not PAH, it is expected that the negative control interferometer will show significantly less change compared to the biotin coated target interferometer.

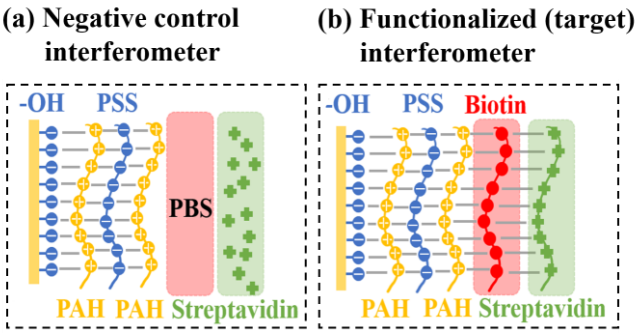

Fig. 37: Both sensors were coated with PAH-PSS-PAH layer by layer nanofilms. (a) PBS negative control interferometer and (b) biotin functionalized (target) interferometer.

2.5 Results

2.5.1 Temperature sensing

To characterize the temperature sensitivity, the temperature of the sensors was increased from 25℃ to 60℃ and the results are shown in Fig. 38. The phase sensitivity to temperature was measured to be -0.15 rad/℃ at 26℃, noting that temperature change in the laboratory is estimated at approximately ±1℃ during the time frame of sensing experiments (two hours). Such a potential phase change of ±0.15 rad is small compared to the RI sensing demonstration [Fig. 40], but potentially hinders biochemical sensing as the predicted sensitivity for nanometer scaled coatings is in the order of only 0.01 rad/nm [Fig. 28].

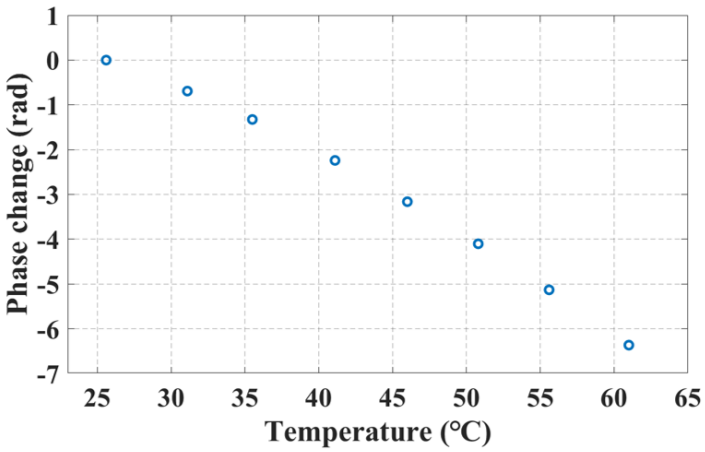

Fig. 38: Phase change for a 174 µm interferometer from 25°C to 60°C.

To eliminate the phase change from ambient temperature changes, the experiments were conducted within the water tank with a fixed temperature. The phase change in the water tank over two hours (time needed for the whole functionalisation and streptavidin sensing experiment as described it Sec. 2.4.2 B) for a 174 µm interferometer was measured and the results are shown in Fig. 39. The solid line is the average value and the coloured box corresponds to three times the standard deviation (±3σ). By using the water tank, the phase change from the external temperature change can be reduced to approximately 0.015 rad, which corresponds to approximately 1.5 nm coating thickness.

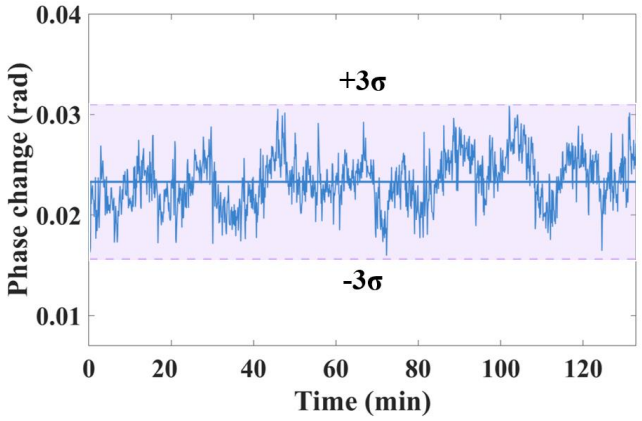

Fig. 39: Phase change of 174 µm interferometer due to the temperature change.

2.5.2 RI sensing

A. Single interferometers

The single interferometer RI sensing results were obtained by filling the interferometers with a serial of NaCl solutions with different concentration (0% to 10% in steps of 1 %). The phase changes of the corresponding reflection spectra and FFT peaks were monitored by the interrogator. Fig. 40 demonstrates the sensing results for 94 µm and 178 µm interferometers respectively.

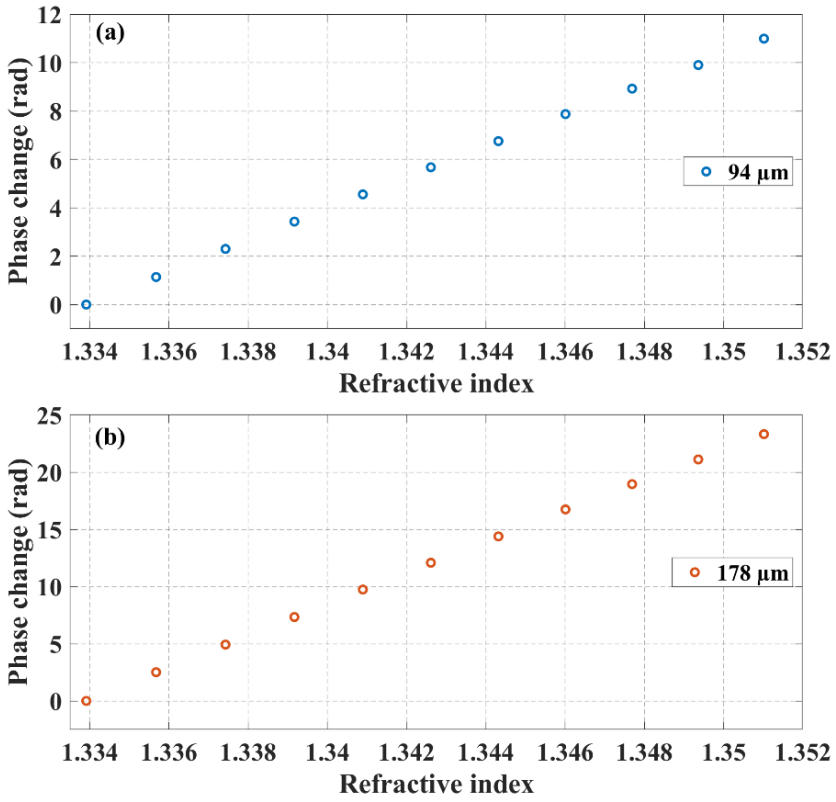

Fig. 40: RI sensing results for (a) 94 µm and (b) 178 µm interferometers.

Fig. 40 demonstrates that the RI sensitivity of the 94 µm and 178 µm interferometers are calculated as 1972 nm/RIU and 2200 nm/RIU, respectively. Fig. 40 also demonstrates that the phase sensitivity is proportional to length of the interferometer. For the longer interferometer, the phase change from the same RI change is larger than that of the shorter interferometer. This can be attributed to that longer cavity provide longer sensing area. The results demonstrated in Fig. 40 matches the interference spectrum as derived in (35), where phase is directly related to interferometer length.

B. Multiplexed RI sensing

To demonstrate multiplexed RI sensing, NaCl solutions were pumped into one of the interferometers while water was pumped into the other, and vice versa. The phase change at the two Fourier frequencies corresponding to the two interferometers were simultaneously monitored with respect to the RI change. In this way both RI change inside one interferometer as well the RI crosstalk on the other interferometer was monitored.

Fig. 41(a) shows the case where NaCl solutions were pumped into the 80 µm interferometer and water was pumped into the 183 µm interferometer. It is clear that the phase of the 80 µm interferometer shifted due to the change in concentration of the NaCl solution (the change in RI). Meanwhile, the phase of the 183 µm interferometer was constant, indicating that the crosstalk between those two interferometers was negligible.

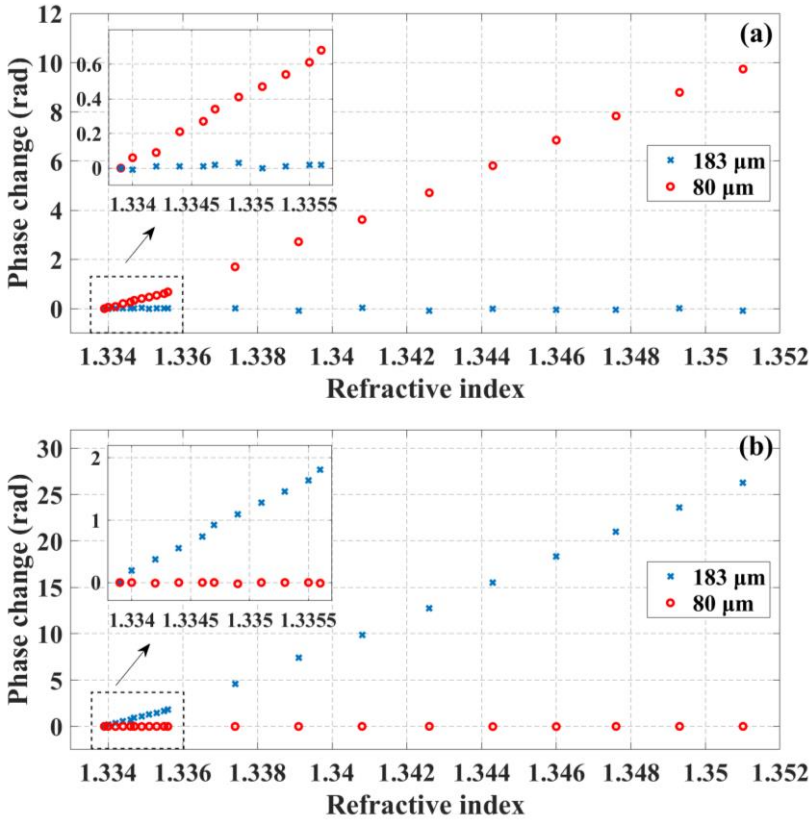

Fig. 41: RI sensing results for the 80 μm and 183 μm dual interferometer. (a) NaCl solution in the 80 μm interferometer; (b) NaCl solution in the 183 μm interferometer.

Similar results were obtained in the case where NaCl solutions were pumped into the 183 μm interferometer and water was pumped into the 80 μm interferometer, as shown in Fig. 41(b). The phase sensitivity of the interferometer with respect to RI is seen to be closely related to the interferometer lengths. Note that the slopes of the two phase change lines, 0.1% to 1% and 1% to 10%, are slightly different due to a small error between the two sets of NaCl serial dilutions. These results illustrate that the crosstalk between the multiplexed C-shaped fibre-based FPIs is negligible, paving the way for using the proposed sensors for multiplexed biochemical sensing.

2.5.3 Biosensing

For biochemical sensing experiments, the sensors were put into a temperature controlled waterbath to maintain a temperature stable environment.

To demonstrate biochemical sensing, dual interferometers were coated with PAH-PSS-PAH layer by layer nanofilms (see Sec. 2.4.2-B). Subsequently, one of the interferometers were functionalized with biotin molecules, while the other interferometer was left in PBS buffer without biotin to serve as a negative control. A streptavidin solution was then utilized to check the response of the target (biotin coated) interferometer compared to the negative control (no biotin) interferometer. The process was applied to three pairs of interferometers and the resulting phase shifts, after rinsing with PBS solution to remove any unbound biotin/streptavidin molecules, are shown in Fig. 42.

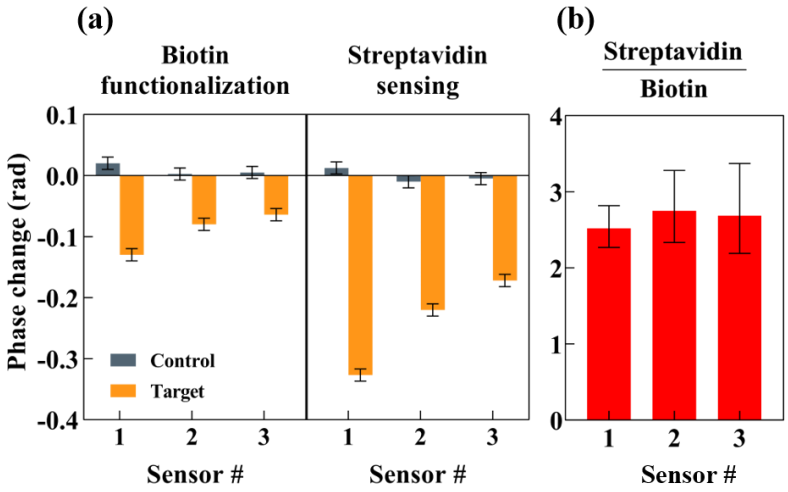

Fig. 42: (a) The phase change for the control and target sensors during the biotin functionalization and streptavidin sensing processes. (b) Streptavidin/Biotin ratios. Error bars represent the 3σ noise of 0.01 rad from Fig. 39.

The experiments were repeated three times with 90 (control)/188 (target) μm (sensor 1); 82 (control)/183 (target) μm (sensor 2) and 340 (control)/92 (target) μm (sensor 3) dual interferometers, respectively. The phase clearly decreased following biotin functionalization, indicating that the biotin molecules were successfully attached to the polyelectrolyte nanofilms. In all cases, only the interferometers that were functionalized with biotin showed a significant change in phase, indicating that the streptavidin successfully bound to the biotin molecules and the other interferometer correctly served as a negative control.

It is observed that different interferometers, independent of cavity length, show different phase changes for the biotin and streptavidin steps. This is likely due to different polyelectrolyte coating density as a result of uncontrolled surface charge density. However, the streptavidin/biotin phase change ratios [Fig. 42(b)] were observed to be consistent between the three dual-interferometer systems, indicating the potential of our dual cavity interferometer to act as a quantitative biochemical sensor.

2.6 Discussion and conclusions

We have demonstrated that interferometers fabricated with C-shaped fibres are a simple and effective method for high sensitivity RI-based sensing and have good multiplexing ability that can be utilised for biochemical sensing. The interferometers can be monitored with a standard optical sensor interrogator, which yields clear interference spectra. A single interferometer system can be monitored directly through its intrinsic FFT Fourier frequency. The dual interferometer system can form a modulated spectrum that can be de-multiplexed through FFT followed by monitoring the phase of each interferometer individually.

Serially multiplexing additional interferometers can provide greater ability to achieve

appropriately controlled multi-parameter biochemical sensing. However, this adds complexity in terms of separating their Fourier frequencies and must be appropriately designed so that sufficient reflection can be obtained from the remote interferometers. As the interferometers are open and not guided, the beam is divergent inside the interferometers, leading to increased loss if the cavity length is increased, which ultimately limits the cavity length to several hundred microns and limits the multiplexing capability to a few cavities.

Another limitation relates to the minimum cavity length that can be used. The shortest interferometer made within our laboratory is approximately 25 μm. In this case, the reflection signal is stronger due to reduced beam divergence related loss. However, the shorter interferometer corresponds to a larger free spectral range, making the demodulation using FFT more difficult. A broader bandwidth light source could allow correspondingly shorter cavities to be utilized, reducing their loss and allowing an increased number of serially multiplexed cavities.

Another factor to consider is that the proposed sensor is sensitive to temperature as the cavity is filled with liquid with a relatively high thermo-optic coefficient. We measured a phase sensitivity to temperature of -0.15 rad/°C for a water-filled 174 μm interferometer. To stabilize the temperature, we performed our measurements within a water tank. Under this condition a phase noise (3σ) of 0.01 rad was measured (Fig. 39), which is likely due to residual temperature fluctuations and stability of the optical sensor interrogator. This noise correlates to a detection limit of 6.5×10^{-6} RIU, which is comparable to other reported interferometer-based optical biosensors (e.g. 3.8×10^{-6} RIU in [25]). As a biochemical sensor, the 0.01 rad noise correlates to a detection limit of 61 μg/mL for our example protein streptavidin. For sensor operation with these detection limits in an environment with lesser means of temperature control, e.g. in-field measurement, the temperature influence would need to be compensated, such as using an FBG or by utilizing an inter-cavity interferometer of appropriate length to act as a reference temperature sensor.

Chapter 3 Optical fibre microcavity dye laser with specialty fibres

3.1 Introduction

In this chapter, C-shaped fibres and exposed core fibres (ECF) are investigated for their potential use in fabricating microfluidic dye lasers. Just as with biochemical sensing, microfluidic optical fibre devices have potential for low volume operation and easy interchange of fluids. The advantage for use in a laser configuration is the potential to readily exchange the gain media to prevent photobleaching of fluorescent dyes and potential for creating tuneable sources.

Both C-shaped fibres and ECFs can be utilised to fabricate open cavities as microfluidic devices for potential laser operations. The C-shaped fibre only functions as a capillary where the pump light transmitted through the lead-in fibre diverges along propagation and then couples into the lead-out fibre. The pump light can directly propagate through the gain medium filled inside the C-shaped fibre cavity. However, due to the beam divergence, the length of the C-shaped fibre cavity is limited to only hundreds of microns, which corresponds to higher lasing threshold.

Compared with the C-shaped fibre, ECF can guide light inside the fibre core and the tail of the guided light can extend to the open side. This guided light tail (*i.e.* evanescence field) can then be utilised to excite the gain medium to potentially obtain lasing. The generated emission is coupled back to the fibre core which is then coupled to the lead-out fibre for measurement. As a waveguide, the length of ECF can be longer than the C-shaped fibre to reduce the lasing threshold. However, the evanescence field is weak and raises the lasing threshold unless sufficiently long optical fibre is used.

In this project, both C-shaped fibre cavities and ECF cavities have been investigated to obtain lasing with an external mirror resonator. The gain medium adapted was rhodamine B solutions dissolved in water and ethanol with different concentration. In Sec. 3.2, the fabrication of optical fibre cavities for C-shaped fibre and ECF are first introduced. After that, the details of the experimental method are provided. In Sec. 3.3, the theoretical background such as fibre characterisation, optimal length of the cavities, concentration of the dye solutions, dye photobleaching and lasing threshold are described. The results are then presented in Sec. 3.4.

To clarify the terminology used in this chapter: C-shaped fibre cavity refers to the cavity formed by the C-shaped fibre and the lead-in/out fibres; C-shaped fibre cavity flow cell refers to the C-shaped fibre cavity plus the glass capillary; laser cavity refers to the resonator formed by the two mirrors.

3.2 Fabrication and experimental method

3.2.1 Fabrication

The optical fibre cavities that were fabricated with ECFs and C-shaped fibres are shown in Fig. 43. The ECF or C-shaped fibre was first spliced with a lead-in conventional step index fibre. Three different lead-in fibres were tested: single mode fibre at visible wavelength (SMF450, *d*=3.5 µm, MFD=3.5 µm, Thorlabs), few-mode fibre (SMF28, *d*=8.2 µm, MFD=6.1 µm, Corning) and multimode fibre (FG050LGA, *d*=50 µm, MFD=50 µm, Thorlabs). The ECF or C-shaped fibre was then cleaved with certain length. Then the cleaved ECF or C-shaped fibre was spliced to a lead-out fibre to capture the generated emission from the fibre cavities. Both C-shaped fibre cavities and ECF cavities are packaged inside a glass capillary to form flow cells. The inlet and outlet can be connected to an external peristaltic pump to facilitate dye circulation.

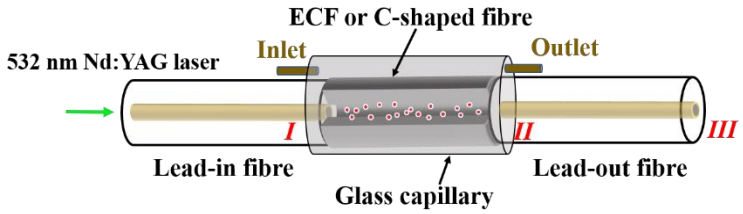

Fig. 43: A flow cell based on a C-shaped fibre cavity or an ECF cavity combined with lead-in and lead-out fibres. The flow cell was fabricated with inlet and outlet for liquid circulation. The mark I, II and III are three monitoring points during the ECF cavity flow cell fabrication.

The fabrication process of the C-shaped fibre flow cells in this project is similar to that demonstrated in Fig. 29. However, due to the complicated cross-sectional structure of the ECF (as in Fig. 44.), the cleaving and splicing for the ECF flow cells are different in terms of cleaving tension and splicing program setup, which can both affect the coupling efficiency between the ECF and the lead-in/out fibres. In this project, two core size ECFs were investigated to fabricate fibre cavities: 1.8 µm and 7 µm core ECFs. The parameters (Fujikura FSM-100P) for splicing the 1.8 µm and 7 µm core ECFs to the lead-in/out fibres are shown in Table 3 and the standard (STD) arc current in this project was approximately 15.6 mA.

Table 3: Cleaving and splicing setup for exposed core fibre flow cells

	Arc time (ms)	*Arc current (mA)*	*Cleaving tension (g)*
1.8 µm core	3500	STD - 3.3	230
7 µm core	3500	STD - 4	200

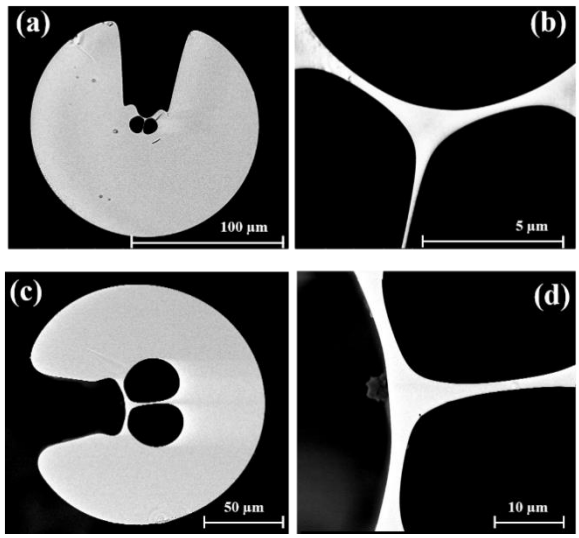

Fig. 44: (a) Cross-section image of 1.8 µm core ECF and (b) its core area; (c) Cross-section image of 7 µm core ECF and (d) its core area.

The key challenge in fabricating the ECF flow cell is to make sure that enough light can be coupled into the fibre. During the fabrication, the ECF was first spliced with a lead-in fibre and then cleaved with the desired length. The output pattern from the ECF was then checked by imaging the fibre output (at mark point *II* as labelled in Fig. 43) using a lens. A 630 nm red laser was utilised to check that light was guided inside the ECF core. After that, another lead-out fibre was spliced with the ECF. The input and output powers (at mark point *I*, *II* and *III* as labelled in Fig. 43) were simultaneously monitored during the fabrication to obtain optimal coupling efficiency for the whole flow cell. The coupling efficiency from lead-in fibres to approximately 10-15 cm ECFs (CE 1) and of the whole optical fibre cavities (CE 2) are shown in Table 4 and the measuring points *I*, *II* and *III* correspond to the labels in Fig. 43. Similar result for a cavity fabricated with 150 µm C-shaped fibre is also shown in Table 4.

Table 4: Output power monitored from different lead-in fibres

	10-15 cm ECF				
	I	***II***	***III***		
	SMF450	**1.8 µm**	**SMF450**	**CE 1**	**CE 2**
1	280 µW	100 µW	8 nW	35.7%	<0.01%
2	250 µW	140 µW	10 nW	56.0%	<0.01%
3	220 µW	130 µW	26 nW	59.1%	<0.01%
	SMF28	**1.8 µm**	**SMF28**	**CE 1**	**CE 2**
4	660 µW	35 µW	<1 nw	5.30%	<0.01%

5	620 µW	23 µW	<1 nW	3.71%	<0.01%
6	700 µW	45 µW	<1 nW	6.43%	<0.01%
	SM450	**7 µm**	**SM450**	**CE 1**	**CE 2**
7	300 µW	120 µW	20 µW	40.0%	6.67%
8	380 µW	28 µW	5 µW	7.37%	1.31%
9	350 µW	140 µW	25 µW	40.0%	7.14%
	SMF28	**7 µm**	**SMF28**	**CE 1**	**CE 2**
10	7.3 mW	1 mW	500 µW	13.7%	6.85%
11	7.5 mW	1.35 mW	1 mW	18.0%	13.3%
12	7.5 mW	2.2 mW	1.5 mW	29.3%	20.0%
	FG050LGA	**7 µm**	**FG050LGA**	**CE 1**	**CE 2**
13	12 mW	7 mW	1.5 mW	58.3%	12.5%
14	15 mW	6.5 mW	2 mW	43.3%	13.3%
15	14 mW	8.1 mW	2 mW	57.9%	14.2%

150 µm C-shaped fibre

	FG050LGA	**7 µm**	**FG050LGA**	**CE 1**	**CE 2**
16	3.8 mW	2.8 mW	2.64 mW	73.7%	69.5%

From Table 4, data 1-6 shows that for a 10-15 cm long 1.8 µm ECF, SMF450 and SMF28 can deliver reasonable amount of pump light into the ECF cavity as lead-in fibres. However, most of the light is significantly lost after splicing the lead-out fibres with the ECF. Data 7-15 shows that for a 10-15 cm long 7 µm ECF, all three classes of lead-in fibres can provide good coupling efficiency. However, due to the relative large core size, the coupling efficiency from pump laser to the lead-in fibres are significant larger when using SMF28 and FG050LGA as shown in Table 4. As a result, SMF28 and FG050LGA are used as lead-in/out fibres in this project. For the 150 µm C-shaped fibre, the FG050LGA is suitable as lead-in/out fibres.

3.2.2 Laser configuration

In this project, a laser configuration based on an external mirror resonator was adapted as

demonstrated in Fig. 45. A Q-switched Nd:YAG laser (Quanta Ray INDI series, Spectra-Physics, Newport Corporation) at 532 nm was utilised for optical pumping. The laser can deliver 5-8 ns pulses (circular beam) with maximum energy of 160 mJ at a repetition rate of 20 Hz, which corresponds to a maximum average power of 3.2 W. Besides the pulsed-laser mode, the laser can also be operated at long-pulse mode, which has much longer pulse and lower pulse energy compared with pulsed-laser mode. The long-pulse laser is essentially continuous-wave laser and it is used for configuration optimising and fluorescence measurement in this project. Accordingly, the pulsed laser mode is utilised to obtain lasing.

As shown in Fig. 45, the laser beam from the pump laser was first reflected by two mirrors M_1 and M_2 to change the height and propagating direction. The two lenses L_1 (focal length f_1=3 cm) and L_2 (focal length f_2=10 mm) then decreased the laser beam size from 1 cm to 3.3 mm. After that, the laser beam was reflected again by mirror M_3 and dichroic mirror DM and then coupled into the lead-in fibre and the flow cell formed by C-shaped fibre or ECF. The objective lens O_1 (magnification: 10 times; effective focal length: 18 mm, Thorlabs for SMF-28 or magnification: 4 times; effective focal length: 45 mm, Thorlabs for FG050LGA) reduces the beam size to a value that is compatible to the mode field diameter of the lead-in fibre for better coupling. The flow cell was filled with Rhodamine B solution (dissolved in water or ethanol) as the gain medium. To facilitate the dye circulation, the flow cell was connected to an external peristaltic pump. In this project, different concentrations of dye were tested to obtain optimal absorption of optical pumping. The influence of fibre length was also investigated later in the theoretical analysis section (Sec. 3.3).

In addition, the generated emission in the flow cell was coupled into the lead-out fibre, which was then collimated by an objective lens O_2. Afterwards the collimated light was split into two parts by a cubic beam splitter BS (50:50). Note that in future a 90:10 beam splitter could be used as it corresponds to a lower lasing threshold. However, due to the low coupling efficiency as discussed in Sec. 3.2.1, we increased the reflected part for better fluorescence measurement. This reflected light was then attenuated by the neutral density mirror ND (ND=0.5 to 2) before it was measured with a spectrometer (iHR550, Horiba Scientific) to protect the spectrometer. In addition, the residual pump laser was filtered by the long pass filter. In this configuration, the generated emission was amplified in the laser cavity formed by the two external mirrors M_4 and M_5.

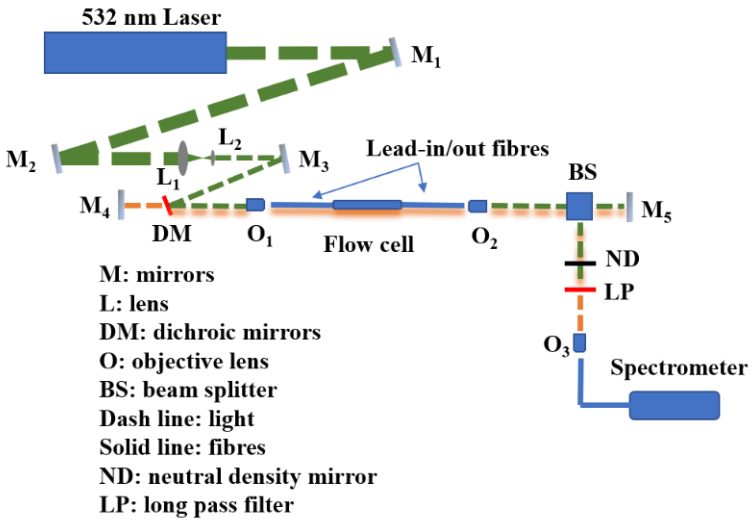

Fig. 45: Laser configuration based on an external mirror resonator.

3.3 Theoretical analysis

Based on the laser configuration proposed in Fig. 45, the feasibility of achieving lasing with C-shaped fibre cavity and ECF cavity was analysed in the following aspects: modal characterisation of C-shaped fibres and ECFs, coupling efficiency of the fibre flow cells, damage threshold of fibres, specialty fibre length, dye concentration and dye photobleaching.

3.3.1 Fibre modal characterisation

A C-shaped fibre is simply a capillary with an open hole for solution circulation. As a result, the light propagating inside a C-shaped fibre diverges through the fibre and is not guided. Conversely, ECFs are microstructured waveguides that can support various propagating transverse modes depending on the fibre configuration such as the fibre geometry and refractive index difference between the fibre core and open holes. As discussed in Chapter One, for the ECFs, an evanescence wave extends into the open holes, which can be used for sensing or interaction with a gain medium for lasing. The fraction of energy that propagates in evanescence wave can be manipulated by changing the fibre geometry such as core radius or RI of the medium inside the open hole.

In this section, ECFs with 1.8 µm and 7 µm core diameters were evaluated to determine the fraction of energy that propagates within the evanescent field and is thus available to interact with the gain medium. ECFs with these core diameters have previously been fabricated at the University of Adelaide with silica glass (RI 1.45885, F300 HQ, Heraeus Quartzglass) [75, 76]. The ECFs were simulated using the finite element method (COMSOL 5.4). The cross-sectional images of 1.8 µm and 7 µm core ECF are shown in Fig. 46 (a) and (d). Their fundamental modes with two orthogonal polarisations are shown in Fig. 46 (b), (c) and (e), (f) respectively.

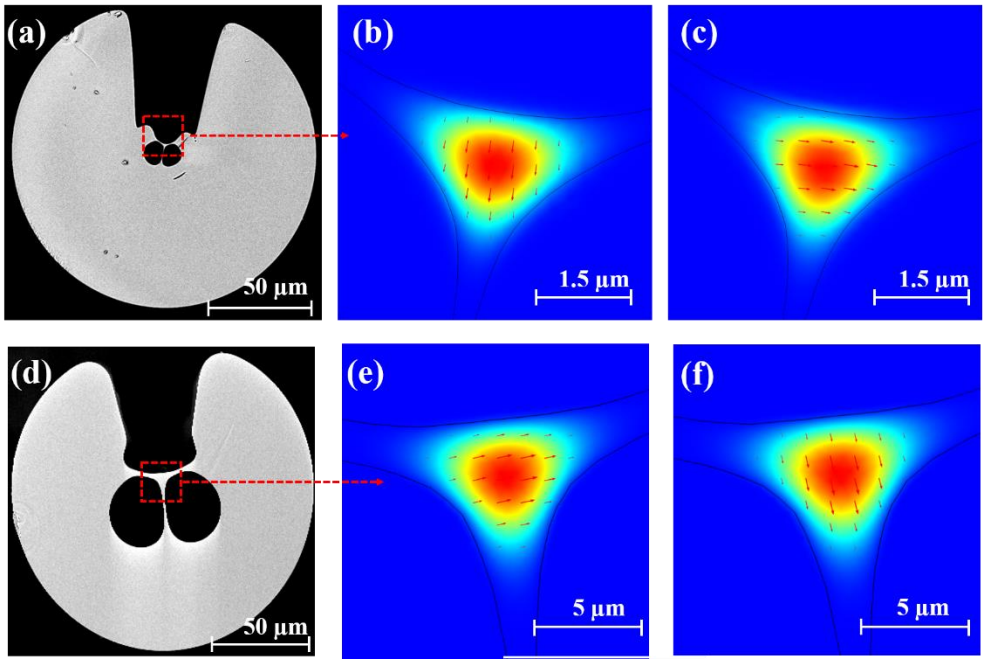

Fig. 46: Cross-section image of (a) 1.8 µm core ECF and (d) 7 µm core ECF; fundamental modes with two polarisation of 1.8 µm ECF (b),(c) and of 7 µm core ECF (e), (f) with air in all three holes.

Compared with the modal distribution of single mode fibres as in Fig. 3, the original circular Gaussian beam shape is deformed due to the fibre geometry. As demonstrated in Fig. 46, for both polarisations the tail of the guided fundamental mode extends into the open side. This can be attributed to refractive index contrast between the ECF core and the open hole [77]. To increase the evanescence wave, one method is to increase the refractive index of the medium inside the open hole. The modal distributions and effective refractive index n_{eff} of each mode with different refractive index n inside the open hole are shown in Fig. 47.

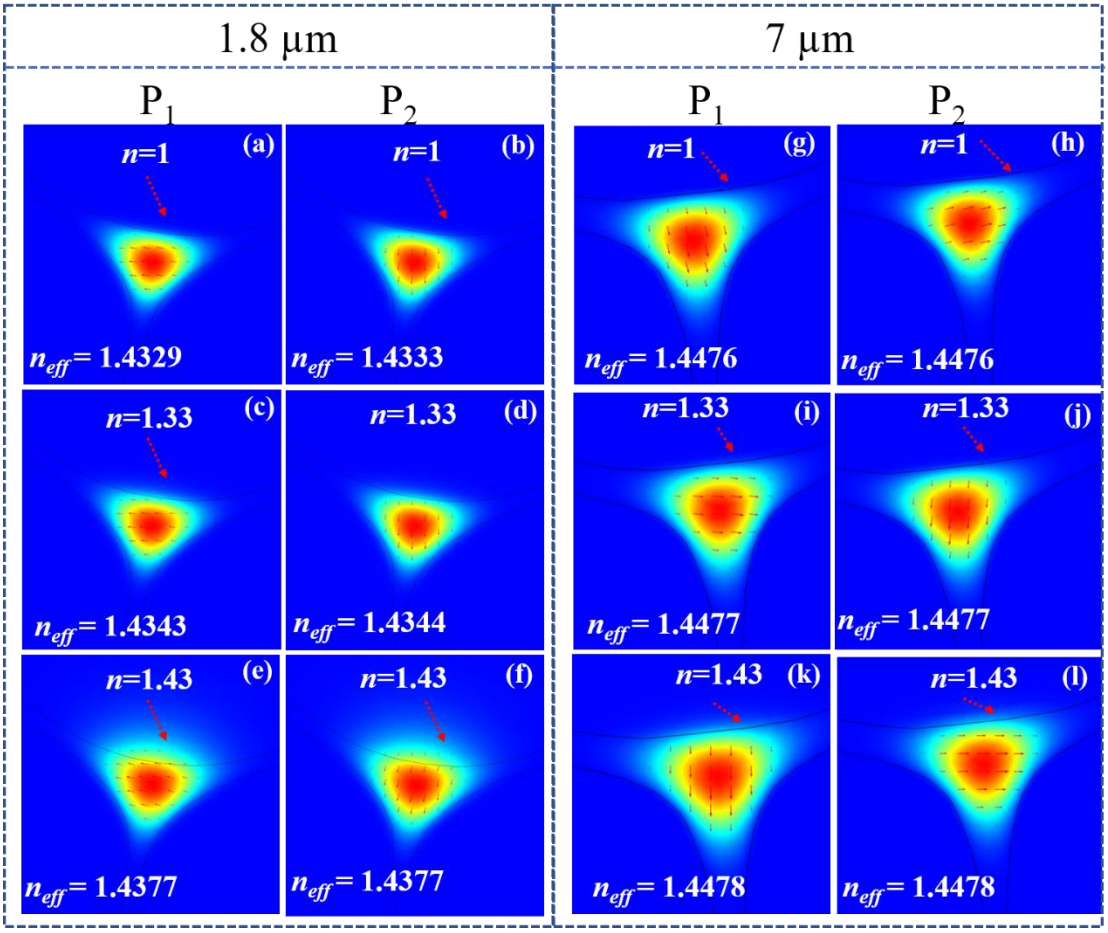

Fig. 47: Fundamental mode with two polarisation for the 1.8 µm ECF: (a) and (b) are with air (n=1); (c) and (d) with water (n=1.33); (e) and (f) with dye (n=1.43). Fundamental mode with two polarisation (P_1 and P_2) for the 7 µm ECF: (g) and (h) are with air (n=1); (i) and (j) with water (n=1.33); (k) and (l) with dye (n=1.43).

Fig. 47 demonstrates that when filling the open hole with higher refractive index medium (*i.e.* smaller refractive index contrast between the medium and the fibre core), the fraction of modal energy in the evanescence wave increases. The fraction of modal energy on the evanescent wave (termed power fraction, PF) can be written as:

$$PF = \frac{\int_H S_z(\vec{r})dS}{\int_A S_z(\vec{r})dS} \tag{74}$$

where S_Z refers to the Poynting vector in the z-axis; H and A are the gain medium area and the whole fibre cross-sectional area, respectively. Note that the power fraction of ECF also corresponds to the coupling efficiency of the generated emission from the evanescence wave area of the ECF to the fibre core. Combining the results obtained from COMSOL simulations, the power fraction for 1.8 µm core ECF and 7 µm core ECF when filling the open holes with different concentration medium for the two polarisations (P_1 and P_2) are shown in Table 5.

Table 5: Power fraction for 1.8 µm core ECF and 7 µm core ECF when filling the open holes with different concentration medium. P_1 and P_2 refer to the two polarisations.

RI of open hole / Core size (µm)	1.00		1.33		1.43	
	P_1	P_2	P_1	P_2	P_1	P_2
1.8	0.18%	0.089%	1.1%	1.2%	13%	14%
7	0.0042%	0.0096%	0.055%	0.044%	0.73%	0.68%

Table 5 shows that when the same RI medium is filled into the 1.8 µm core ECF and the 7 µm ECF core, for example RI=1.43, the power fraction of the evanescence wave of the 1.8 µm core ECF (13.643% and 13.973% depending on polarisation) is significantly larger than that of the 7 µm core ECF (0.7294% and 0.6832% depending on polarisation). These results also reveal that the evanescent field of the ECF can be increased by both decreasing the core diameter or reducing the refractive index contrast between the core glass material and the laser gain solution. While using the 1.8 µm core ECF allows greater interaction with the gain medium, the coupling efficiency has been experimentally demonstrated significantly lower than the 7 µm core ECF in Sec. 3.2.1 during the fabrication. To further understand the trade-offs with coupling efficiency and fibre loss, the theoretical calculation of coupling efficiency for both ECF and C-shaped fibre is introduced in the following sections.

3.3.2 Coupling efficiency

For the C-shaped fibre, the guided light in the core of the lead-in fibre is first transmitted into the open hole at the left interface (I) as shown in Fig. 48, which then diverges along the propagation inside the C-shaped fibre. This light can be then coupled into the lead-out fibre directly at the right interface (II) as shown in Fig. 48.

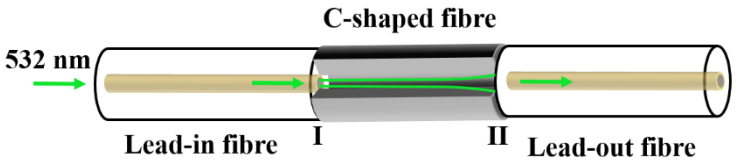

Fig. 48: The divergence inside the C-shaped fibre.

The coupling efficiency for the C-shaped fibres can be simply expressed as in (32) by the mode field diameter (MFD) at the two interfaces, which is directly related to the fibre length. Fig. 49 demonstrates the coupling efficiency for a C-shaped fibre and two single mode fibres as lead-in and lead-out fibres (SMF-28).

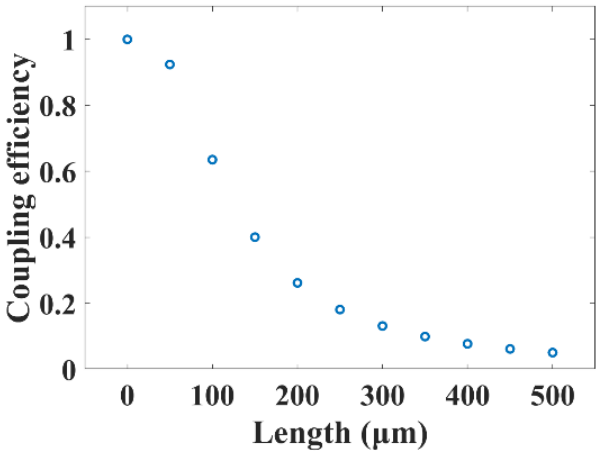

Fig. 49: Coupling efficiency of the C-shaped fibre cavities with singe mode fibre (SMF-28) as lead-in and lead-out fibre with respect to fibre length.

This simplified model can also be used for the ECFs. To get accurate MFD of ECFs, finite element method (COMSOL 5.4) mode simulation results were obtained. The calculation and simulation were based on a silica exposed core fibre (core diameter ~1.8 µm and 7 µm; core refractive index 1.45) filled with dye (refractive index 1.40). For the fundamental mode, the modal spot sizes in x and y direction, w_x and w_y, are given by [78]:

$$w_x^2 = 4\frac{\iint_S (x-x_c)^2 \left|\mathrm{E}_t\right|^2 dxdy}{\iint_S \left|\mathrm{E}_t\right|^2 dxdy} \tag{75}$$

$$w_y^2 = 4\frac{\iint_S (y-y_c)^2 \left|\mathrm{E}_t\right|^2 dxdy}{\iint_S \left|\mathrm{E}_t\right|^2 dxdy} \tag{76}$$

where E_t is the transvers electric field distribution; x and y are position of the field; x_c and y_c are the x and y coordinates of the centre of the field distribution which can be obtained by:

$$x_c = \frac{\iint_S x\left|\mathrm{E}_t\right|^2 dxdy}{\iint_S \left|\mathrm{E}_t\right|^2 dxdy} \tag{77}$$

$$y_c = \frac{\iint_S y\left|\mathrm{E}_t\right|^2 dxdy}{\iint_S \left|\mathrm{E}_t\right|^2 dxdy} \tag{78}$$

Based on these equations, the MFD of the 1.8 µm core ECF and 7 µm core ECF are calculated as 0.76 µm and 4.6 µm, respectively. The corresponding coupling efficiency regarding different lead-in and lead-out fibres can be generally estimated with (32). In most cases, using 1.8 µm core ECF for flow cell can only obtain very low coupling efficiency which is hard to reach

threshold as shown in Table 4. As a result, the following experiments and calculations are based on 7 μm ECF.

3.3.3 Fibre damaging threshold

To reach the laser threshold, sufficiently high intensity optical pumping into the flow cell is required so that population inversion can be established. However, as the pump power is increased light can potentially damage the fibre itself due to the small cross-sectional area of the fibre, especially on the surface between the fibre and air. In this section, damage threshold of different fibres is theoretically estimated to avoid fibre damaging.

An optical fibre can be damaged by both high intensity laser pulses and high intensity continuous wave laser at the incident interface. The general damage threshold of a bare fibre end is listed in Table 6 [79]. Note that for fibres with termination such as a ferrule, the damage threshold is smaller due to the material limitation.

Table 6: Estimated damage for bare optical fibre

	Theoretical damage	***Practical damage***
CW laser	1 MW/cm^2	250 kW/cm^2
Short pulse laser (peak power)	5 GW/cm^2	1 GW/cm^2

The damage threshold is expressed in terms of intensity, which means that the damage threshold is directly related to the mode field diameters of the fibres In this project, three types of fibres are utilised: SMF450 (d=3.5 μm, MFD=3.5 μm), SMF28 (d=8.2 μm, MFD=6.1 μm) and FG050LGA (d=50 μm, MFD=50 μm). Assuming that the beam size of the pump laser can be successfully reduced to the core size of the fibres, the intensity I_c at the interface of the fibres can be calculated as:

$$I_c = \frac{P_p}{\pi(\frac{MFD}{2})^2} \tag{79}$$

where MFD is the mode field diameter; P_p is the peak power and t is the pulse width of the laser, respectively. The theoretical and practical damage threshold for each fibre for pulsed laser is shown in Table 7.

Table 7: Theoretical and practical damage threshold for each fibre.

	Theoretical damage (W)	***Practical damage (W)***
SMF450	481.1	96.21
SMF28	1461	292.2

FG050LGA	9.817×10^4	1.964×10^4

As described in Sec.3.2.2, the Nd:YAG laser used in this project can deliver 160 mJ pulses with 5-8 ns pulse width, which corresponds to 20 MW peak power. From Table 7, the theoretical damage of the fibres can be rapidly reached using the pump power (0.0024%, 0.0073% and 0.49% proportional to the peak power). This can be improved by splicing the fibre end with a short piece of no-core fibre. The no-core fibre can increase the beam size at the fibre-air interface (the red interface as shown in Fig. 50), which can significantly increase the damage threshold. The length of the no-cladding fibre is decided by ensuring that the beam size after propagation in the no-cladding fibre matches the MFD of the lead-in fibre (at the red interface as shown in Fig. 50) using equation (31).

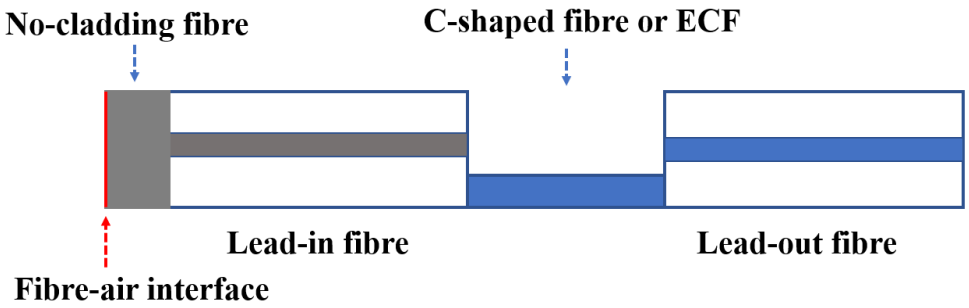

Fig. 50: Splice of the fibre cavity with a short piece of no-core fibre.

3.3.4 Fibre length and dye concentration

When light propagates through a medium, the intensity of the light will be attenuated related to the absorptivity of the medium and the length of the optical path. In the case of ECF, the pump laser in the open hole attenuates while propagating through the dye. The actual attenuation can be affected by the length of the flow cell and the concentration of the dye. In theory, a higher concentration dye and longer flow cell can be adapted to reduce the lasing threshold (this part will be discussed in detail later). However, when the concentration is too high or the flow cell is too long, the laser and the fluorescence will be severely attenuated which makes the detection hard. As a result, reasonable concentration and length need to be calculated in order to reach threshold. The relationship between input and output source when light propagates inside an absorptive medium can be expressed by the Beer-Lambert Law:

$$\frac{I}{I_0}=10^{-\varepsilon c l \eta} \tag{80}$$

where I is the output intensity; I_0 is the input intensity; ε is the molar extinction coefficient of the absorptive medium; c is the concentration; l is the length of the propagation and η is the power fraction (η=1 for the C-shaped fibre flow cells). For Rhodamine B, the extinction coefficient ε is 106000 $cm^{-1}\cdot mol^{-1}$ at 545 nm when dissolved in ethanol [80]. Fig. 51 shows the output/input ratio with respect to different length and rhodamine B concentration for ECF. It shows that the light attenuates much faster when the flow cell is filled with higher concentration

dye. In this project, an output/input ratio of 20% was targeted, where there is significant absorption (80%) for a single pass of the pump but limiting significant losses due to concentration quenching and reabsorption.

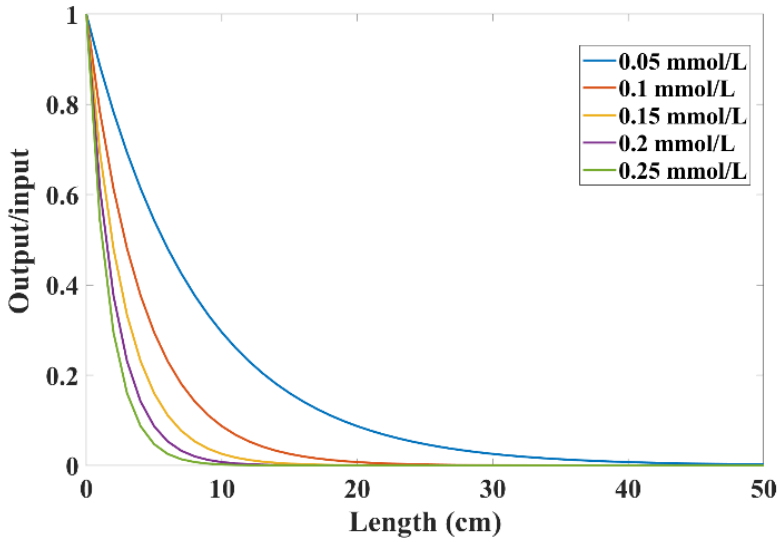

Fig. 51: The output/input ratio with respect to fibre length and rhodamine B concentration for 7 μm core ECF.

For the C-shaped fibre, the light directly propagates through the dye solution which corresponds to a power faction of 1 in this case. Similarly, Fig. 52 shows the output/input ratio with respect to different length and rhodamine B concentration for C-shaped fibres. As demonstrated in Fig. 49, the length of the C-shaped fibre is limited to several hundred microns for reasonable coupling efficiency. As a result, the dye solutions used for C-shaped fibre flow cell normally require higher concentration.

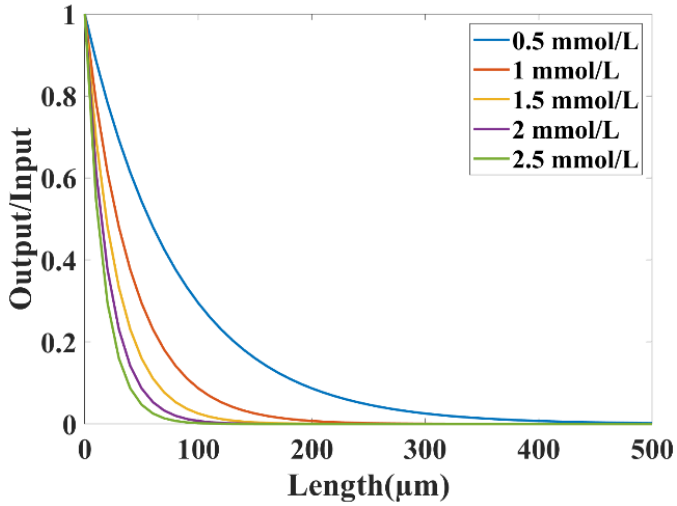

Fig. 52: The output/input ratio with respect to fibre length and rhodamine B concentration for C-shaped fibre.

Note that these results only consider the absorption based on Beer-Lambert law. In practice, the output/input ratio is influenced by the coupling efficiency between the ECF or C-shaped fibre

and lead-in/out fibres.

3.3.5 Dye photobleaching

During the propagation of the laser source, the dye solution absorbs energy from the photons, which can lead to photochemical alteration or photobleaching. This is normally attributed to the cleaving of covalent bonds or fluorophore-molecule interactions. These photobleached molecules cannot be utilised to generate fluorescence afterwards. The photobleaching rate is directly related to the number of photons absorbed, which means a higher intensity pump laser can contribute to a higher photobleaching rate [81]. Combining the photobleaching rate, the actual photobleaching time can be obtained by estimating the total number of molecules in the flow cell. Here the photobleaching rate for the ECF is estimated assuming that all molecules within the flow cell diffuse sufficiently to all interact with the evanescent field. This assumption allows the flow rate in the flow cell to be determined so that photobleaching is avoided.

For ECFs, the quantity of rhodamine B molecules are calculated by estimating the volume of the flow cell while the absorption of the pump laser is characterised by the Beer-Lambert law as discussed in Sec. 3.3.4. Consider a 7 µm ECF, the thickness and width of the evanescence wave are estimated as 0.5 µm and 7 µm, respectively.

Based on the results demonstrated in Fig. 51, the length of the flow cell is set to be 10 cm long and the glass capillary used for flow cell has an inner diameter of 660 µm. In this calculation, the laser intensity is assumed to be its maxima, which is 160 mJ per pulse; the coupling efficiency is set to be 30%; the power fraction of the evanescence wave was calculated as 0.73% for 7 µm core ECF; the circulation of the dye is not considered for this calculation. Fig. 53 demonstrates the photobleaching time for the 10 cm ECF flow cell when it is filled with different concentration dye.

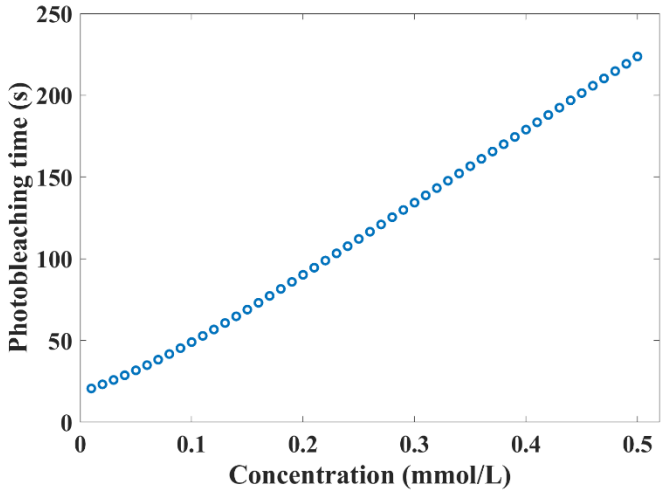

Fig. 53: Photobleaching time of a 10 cm long ECF flow cell with respect to dye concentration.

Fig. 53 shows that even using a very high concentration dye (*e.g.* 0.5 mM), the dye molecules inside the flow cell can be photobleached in a short time (~225 s) when no circulation is applied to the system. As a result, the utilisation of an external pump to provide effective dye circulation

is critical to avoid photobleaching. The actual pump rate can be calculated based on the total dye molecules inside the flow cell. Consider a dye concentration of 0.1 mmol/L, the photobleaching time is calculated to be around 50 s. which means that the pump rate needs to be set as to at least 39.1 µL/min to avoid photobleaching. This can be readily obtained using an available peristaltic pump, which can provide circulation rate up to 100 µL/min. A similar photobleaching calculation is conducted as a function of flow cell length assuming 0.2 mM dye is filled into the flow cell, which is shown in Fig. 54.

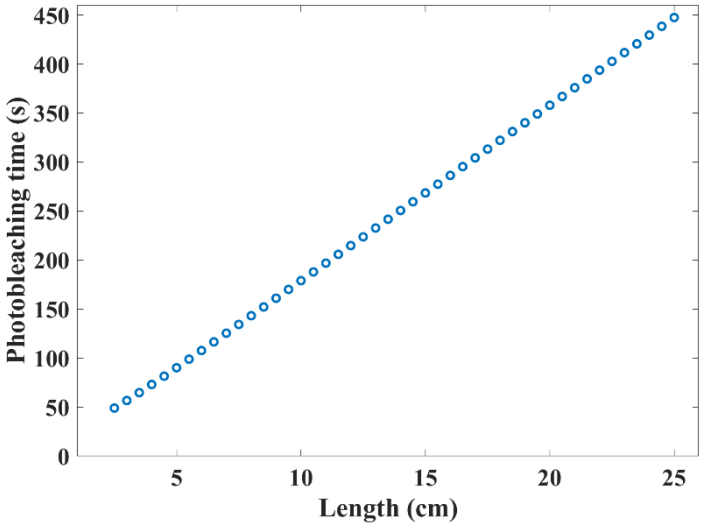

Fig. 54: Photobleaching time of ECF flow cell with 0.2 mmol/L dye with respect to flow cell length.

The same theory and calculation can also be applied to the C-shaped fibre flow cell by adjusting the power fraction and coupling efficiency. For the C-shaped fibre flow cell, although the fibre is only several hundred microns, the flow cell is much longer than that to provide enough dye molecules. The calculation is based on a cavity form with 100 µm C-shaped enclosed in a 10 cm flow cell and the results with respect to different concentration are demonstrated in Fig. 55.

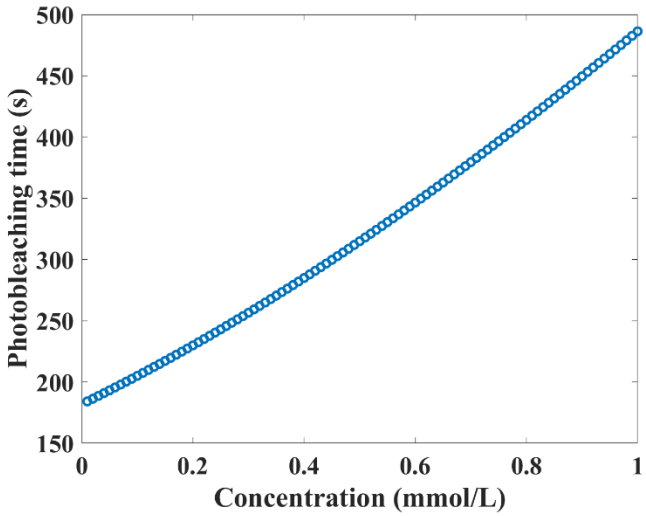

Fig. 55: Photobleaching time of a 100 µm C-shaped cavity enclosed in a 10 cm flow cell with respect to dye concentration.

The results with respect to length of C-shaped fibre is shown in Fig. 56.

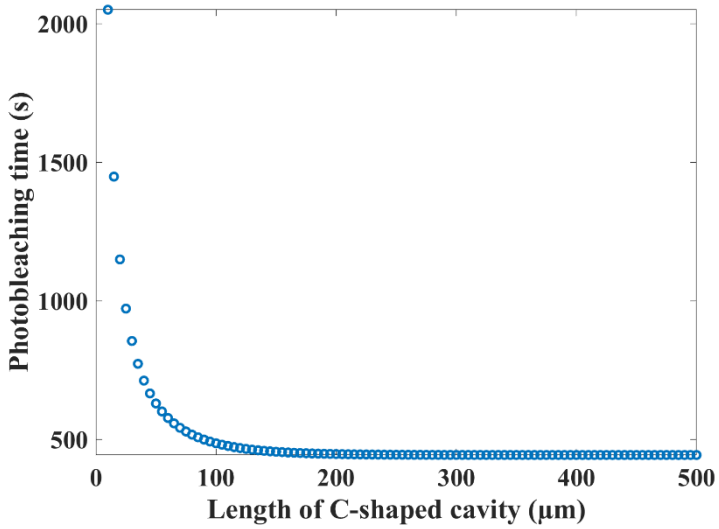

Fig. 56: Photobleaching time of C-shaped cavity enclosed in a 10 cm flow cell with 1 mmol/L dye with respect to fibre length.

For the C-shaped fibres, the flow cell is fixed at 10 cm so that the total amount of dye molecules is constant. When the length of the C-shaped is increased, the actual absorption of pump laser is increased which then reduces the time needed to fully photo bleach the whole flow cell. When the C-shaped fibre is long enough, the absorption reaches 100% and the photobleaching time stays the same as indicted in Fig. 56.

Note that the photobleaching time is calculated assuming that the laser is at its highest energy. However, in practice, the actual laser energy used is well below its maxima due to the limitation of the beam quality and the damage threshold of the fibres. As a result, no obvious photobleaching was observed throughout the experiments.

3.3.6 Lasing threshold

For a Fabry- Pérot type laser resonator laser such as in Fig. 45, the threshold can be derived as [82]:

$$I_{th} = \frac{\gamma h \nu_p d}{\sigma_{em}(\lambda_L)\tau_{sp} L_c} \tag{81}$$

Where γ is the single-pass loss and closely related to specific resonators; h is the Planck constant; ν_p is the frequency of the pump laser; $\sigma_{em}(\lambda_L)$ is stimulated emission cross section at the lasing wavelength λ_L; τ_{sp} is the spontaneous emission lifetime; L_c is the length of the specialty fibre; d is the penetration depth into the dye which can be expressed as:

$$d = \frac{1}{n_0 \sigma_a(\lambda_p)} \tag{82}$$

where n_0 is the ground state population density and $\sigma_a(\lambda_p)$ is the absorption cross section at the

pump wavelength.

For estimating the lasing threshold for the C-shaped fibre and ECF based dye laser, consider the setup as shown in Fig. 45. The single-pass loss can be expressed with three parts: coupling loss, power fraction loss and other losses as in:

$$\gamma = \gamma_{CouplingLoss} + \gamma_{PowerFraction} + \gamma_{Others} \tag{83}$$

The other losses include loss such as the loss at the mirrors, which are typically small. For ECFs, we set 0.1 mM rhodamine B solution as the gain medium and the flow cell is 5 cm long. The lead-in and lead-out fibre are both MMFs with 50 μm core and the coupling efficiency is 30%. For the C-shaped fibres, the flow cell is about 10 cm and the length of C-shaped fibre is 150 μm. The concentration of rhodamine B solution used for C-shaped fibre is 1 mM. The lead-in and lead-out fibre are also 50 μm core MMF and the coupling efficiency is set to be 50%. The remaining parameters used in the calculation can be found in Table 8.

Table 8: Parameters used for lasing threshold calculation.

Speed of light c	3×10^{8} m·s^{-1}
Planck constant h	6.6261×10^{-34} J·s
Pump wavelength λ_p	532 nm
Absorption cross section at the pump wavelength $\sigma_a(\lambda_p)$	3.8×10^{-16} cm^2
Stimulated emission cross section at the lasing wavelength $\sigma_{em}(\lambda_L)$	1.2×10^{-16} cm^2
Ground-state population density n_0	6.022×10^{16} cm^{-3}
Spontaneous emission lifetime τ_{sp}	5 ns

Based on the parameters described above, the threshold intensity is calculated as 1.54×10^{4} W/cm^2 and 1.26×10^{6} W/cm^2 for ECF and C-shaped fibres. The Nd:YAG laser utilised in this project can provide a peak intensity of 9.143×10^{13} W/cm^2 and 1.63×10^{12} W/cm^2 for ECF and C-shaped fibres respectively. This intensity refers to actual intensity that is delivered to the gain medium. In practice, the coupling efficiency needs to be considered. From the discussion in Sec. 3.3.3, the principle limitation is the damage threshold of the fibres. Considering that the damage threshold is 5×10^{9} W/cm^2 for these fibres, the lasing threshold should be readily attainable.

3.4 Results

In this project, lasing phenomenon was not observed with the ECF flow cell. This can likely be

attributed to the limitation of the poor pump laser beam quality, low coupling efficiency into the lead-in fibres, low power fraction (corresponds to low coupling efficiency of generated emission from evanescence wave area to fibre core) and the damage threshold of the lead-in fibres. Therefore, the following discussion focuses on preliminary results obtained with the C-fibre cavity flow cell plus optical characterisation of the rhodamine B gain medium used for these experiments.

In this section, a general rhodamine B fluorescence spectrum obtained by a separate optical setup was first introduced. This spectrum can be further used to verify the spectrum obtained from the laser configuration. After that, the noise obtained during the experiments was discussed and then eliminated by optimising the optical setup.

3.4.1 Rhodamine B fluorescence spectrum

The fluorescence signal of rhodamine B was first measured with a simple configuration as demonstrated in Fig. 57.

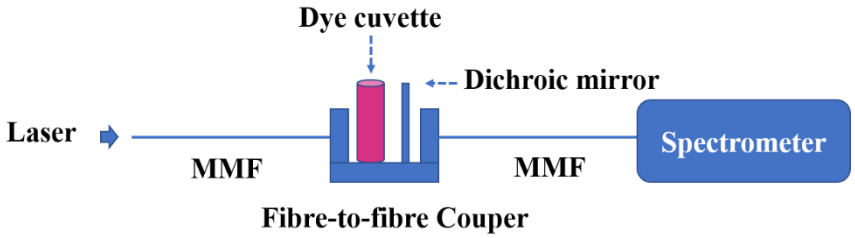

Fig. 57: Optical setup for fluorescence spectrum measurement of rhodamine B solution.

A dye cuvette filled with 0.1 mM rhodamine B solution (dissolved in ethanol) was fixed in an adjustable fibre-to-fibre coupler. The pump laser was delivered with a 50 µm MMF. The residual pump laser was filtered by a dichroic mirror with a cut-off wavelength at 550 nm. The generated fluorescence was captured by a second MMF and measured with an OSA. With this setup, a wide fluorescence spectrum can be obtained as shown in Fig. 58. The fluorescence bandwidth covered approximately 560 nm to 650 nm with a peak wavelength at 588 nm.

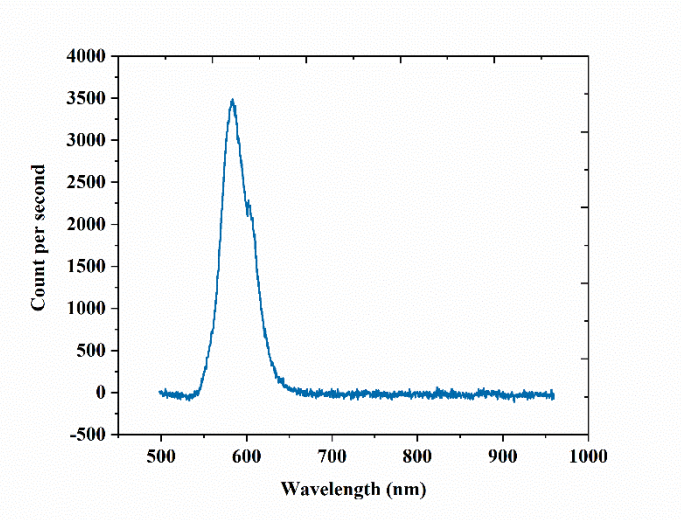

Fig. 58: Fluorescence spectrum for 0.1 mM rhodamine B solution.

3.4.2 C-shaped fibre cavity

A. Fluorescence from fibres

To obtain a fluorescence signal from the flow cells, the configuration shown in Fig. 45 was applied. In all the following preliminary experiments, fluorescence was observed at wavelengths that differed compared to the fluorescence spectrum as shown in Fig. 58.

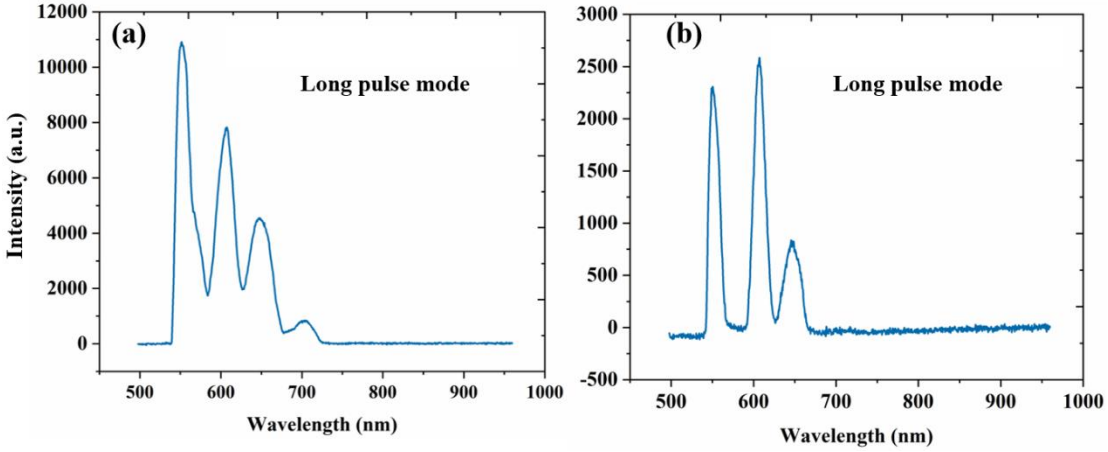

Fig. 59: Fibre fluorescence with 0.1mM dye pumped into (a) fibre cavity fabricated with 70 µm C-shaped fibre and (b) fibre cavity fabricated with 140 µm C-shaped.

Fig. 59 shows the signal measured by the spectrometer with 0.1 mM rhodamine B solution in the (a) fibre cavity fabricated with 70 µm C-shaped fibre and (b) fibre cavity fabricated with 140 µm C-shaped. The lead-in and lead-out fibres for the flow cell are both approximately 1 m long MMF. In Fig. 59(a), four peaks were observed in the cavity with short C-shaped fibre, which reside at 550 nm, 606 nm, 646 nm and 703 nm. The first three peaks were also observed at the corresponding wavelengths in the cavity with longer C-shaped fibre with lower intensity as in Fig. 59 (b). The 550 nm peak is assumed to be the residual intensity from the pump laser as the transmission band for the dichroic mirror is not ideal around the cut-off wavelength. The following peaks at the 606 nm, 646 nm and 703 nm can be likely attributed to the fluorescence or Raman signal generated from the MMFs or the C-shaped fibre cavity flow cell. For the 140 µm C-shaped fibre cavity, the intensity is lower than that in the 70 µm cavity due to that more light being absorbed in the longer cavity.

To confirm that the signal did come from the fibres, several control experiments were conducted. The results are shown in Fig. 60. The measurements in Fig. 60(a) were recorded from a 140 µm C-shaped fibre cavity where no solution was filled in the flow cell. A similar result was also observed when the flow cell was filled with water (solvent for rhodamine B solution) as shown in Fig. 60(b). Fig. 60(a) and (b) indicate that the signal does not come from the dye solution. In Fig. 60(c), the laser was coupled into a 1 m long MMF (lead-in and lead-out fibres), which was then directly connected to the spectrometer. This demonstrates that these signals are actually from the lead-in fibres instead of the flow cell or the C-shaped fibre cavity.

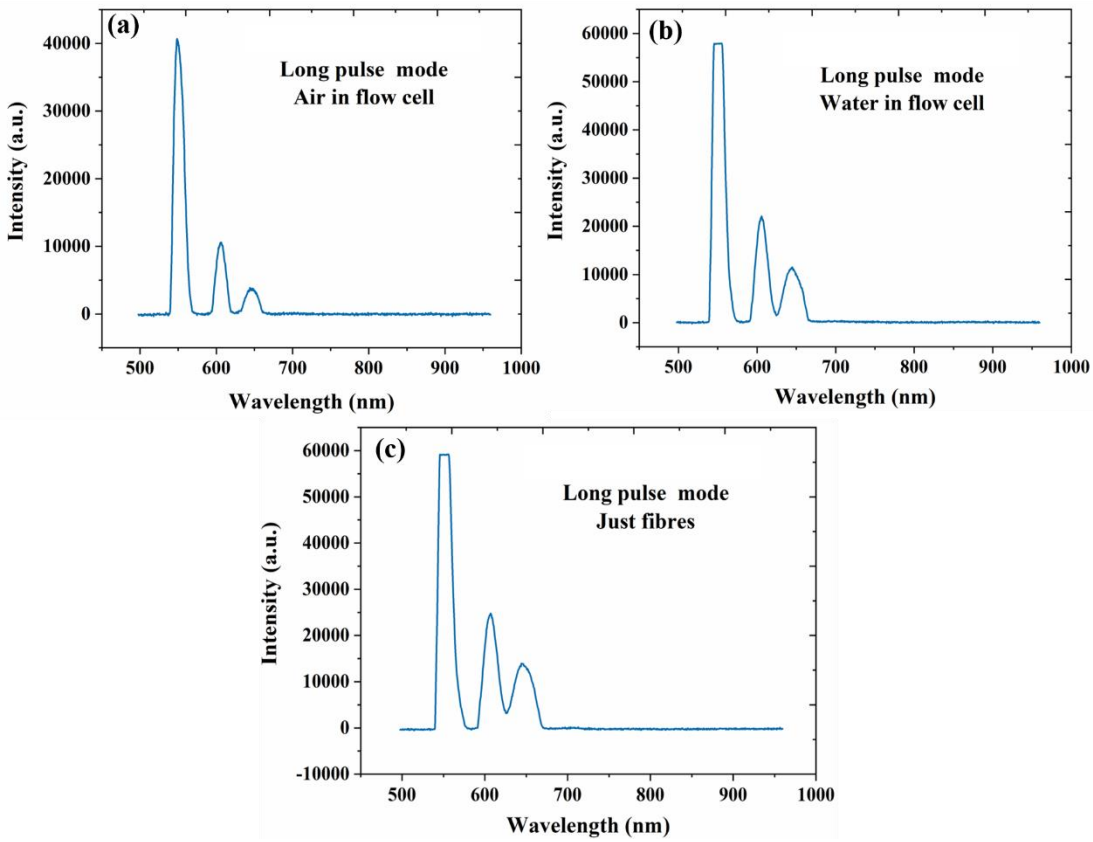

Fig. 60: (a)Signal from a fibre cavity with 140 µm C-shaped fibre, filled with only air; (b) signal from a fibre cavity with 140 µm C-shaped fibre, filled with only water; (c) signal from 1 m lead-in fibre MMF.

Several methods were tested to reduce the background fluorescence signal. In the following experiments, the optical setup used for fluorescence capture was optimised by such as switching different objective lens so that more rhodamine B fluorescence can be obtained by the spectrometer. In addition, the rhodamine B solutions used in Fig. 58 to Fig. 60 was dissolved in water, which has lower pump laser absorption. The rhodamine B fluorescence can be enhanced by changing the solvent to ethanol, which was used for the following tests.

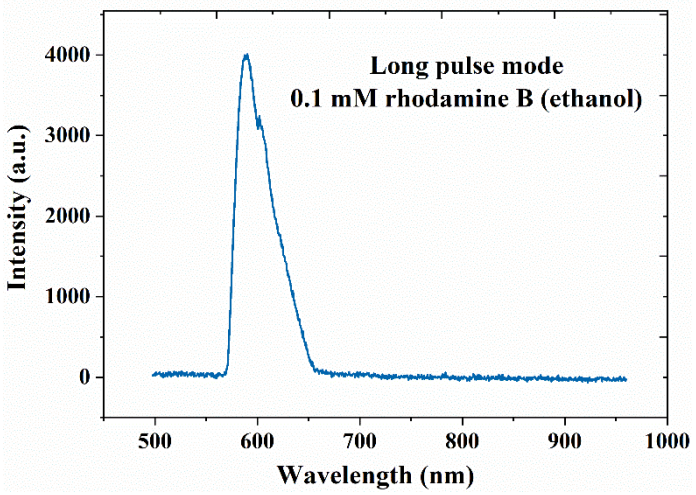

Fig. 61: Fluorescence signal obtained from fibre cavity formed by 140 µm C-shaped fibre

with 0.1 mmol/L rhodamine B solution dissolved in ethanol.

After changing the solvent to ethanol and optimising the optical setup, a clear fluorescence signal can be obtained from C-shaped fibre cavity, which is shown in Fig. 61.

In this experiment, MMF was utilised as lead-in fibre to deliver higher power laser into the C-shaped fibre cavity.

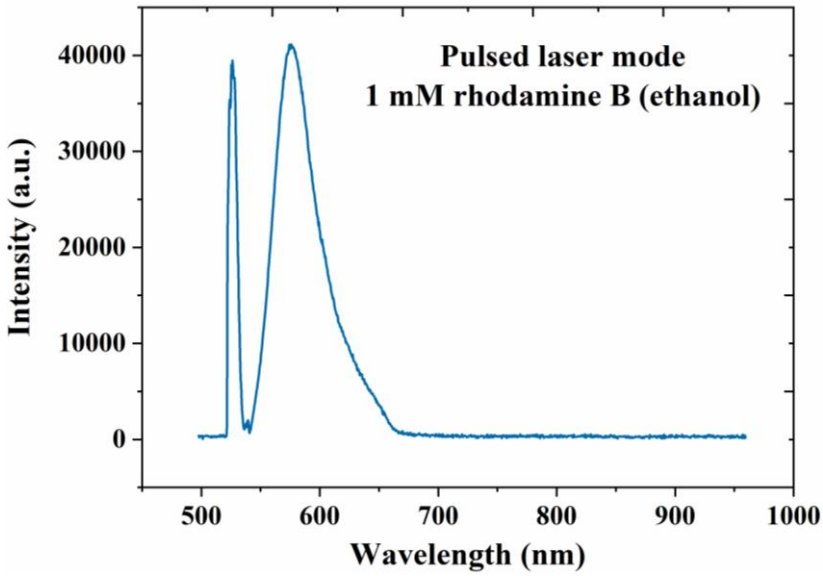

Fig. 62: Fluorescence signal obtained from fibre cavity formed by 140 µm C-shaped fibre with 1 mmol/L rhodamine B solution dissolved in ethanol in the pulsed laser mode.

In Fig. 62, there is a strong signal at around 535 nm, and this can be attributed to the pump laser. In the pulsed laser mode, the peak power of the pump laser can be extremely high, and it can still be measured by the OSA even though a dichroic mirror was applied. In addition, the intensity of the fluorescence has a positive correlation to the pump laser power, which is seen in Fig. 63.

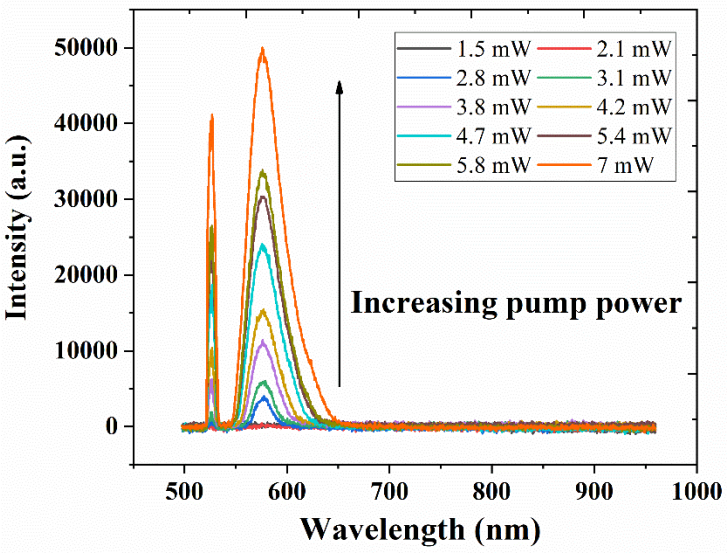

Fig. 63: Fluorescence of fibre cavity formed by 140 µm C-shaped fibre filled with 1 mmol/L rhodamine B solution in the pulsed laser mode.

B. Stimulated emission with C-shaped cavity

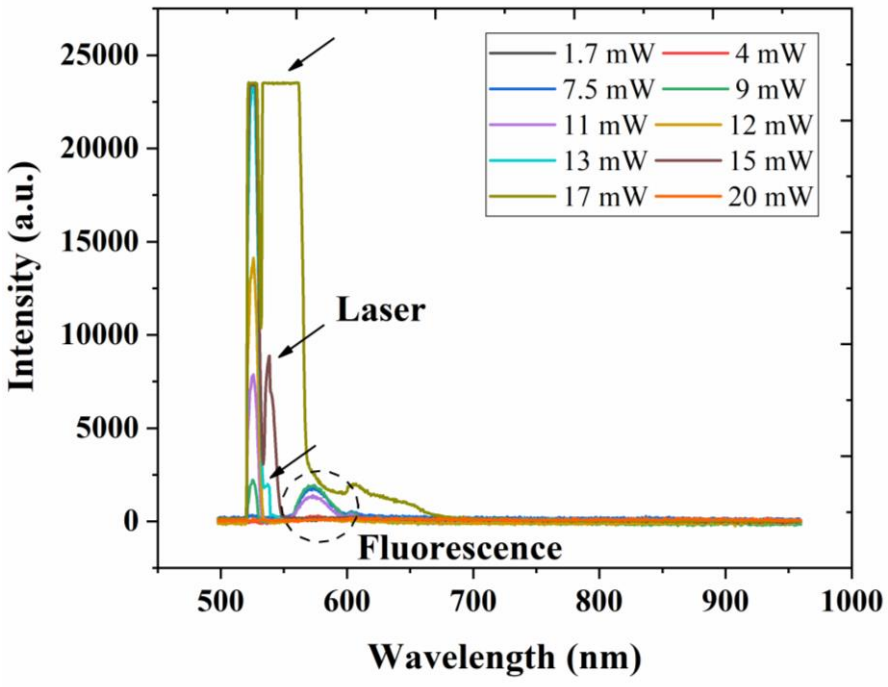

Fig. 64: Stimulated emission phenomenon with C-shaped cavity with MMFs as lead-in/out fibres with increasing average pump power.

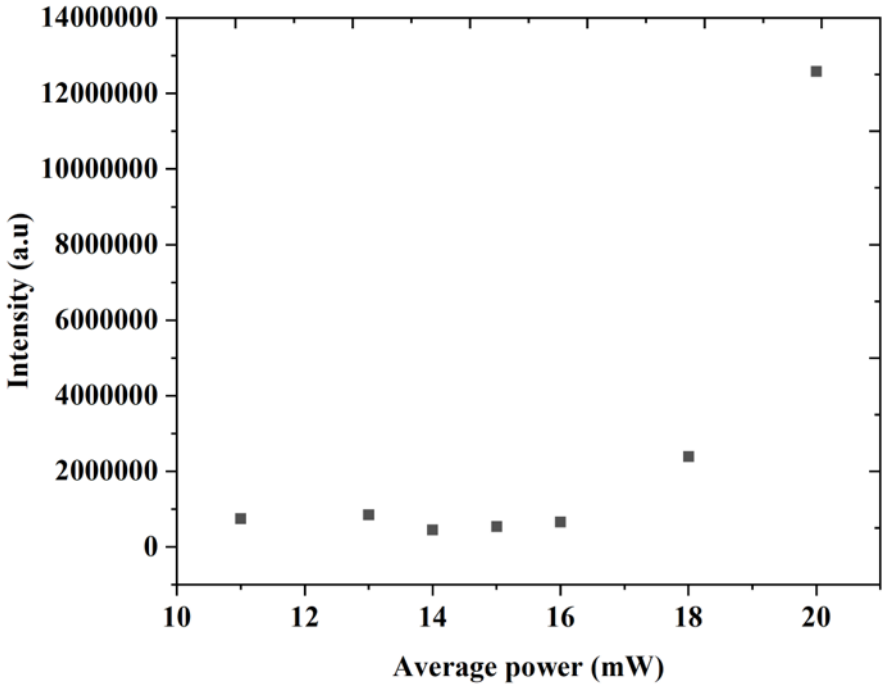

Fig. 65: The intensity of the 539 nm peak with respect to increasing pump power.

During the experiments, a clear threshold phenomenon was observed at 539 nm as shown in

Fig. 64 and Fig. 65, which is attributed to the Raman scattering within the lead-in fibres. In this experiment, MMFs were used as lead-in and lead-out fibres, which can potentially have strong Raman signal. As there are no wavelength selective components in the setup, the Raman signal of the lead-in and lead-out fibre may be amplified by our resonators, which then leads to lasing as demonstrated in Fig. 64. When the lower power pump laser was applied, there was a fluorescence signal observed between 550 nm and 600 nm that matches the rhodamine B fluorescence as shown in Fig. 58. After increasing the pump laser power, the fluorescence signal gradually decreased. Meanwhile, a Raman signal was observed at 539 nm, which is then greatly amplified and exceeded the saturation intensity of the spectrometer. Fig. 64 demonstrates a clear threshold for the 539 nm signal, which is a strong indication that a Raman laser operation was achieved.

The Raman signal is suspected to be from the long MMFs used in this project. As a result, a potential future solution is to reduce the length of the lead-in and lead-out fibres. Furthermore, wavelength selective components can be added into the optical setup to increase the gain of the rhodamine B fluorescence relative to the Raman scattering.

Chapter 4 Conclusion and future work

In this thesis, two applications that utilise specialty fibres to form optical fibre microcavities have been introduced: a multiplexed optical fibre biochemical sensor and an optical fibre dye laser.

Multiplexed biochemical sensing was demonstrated using a dual cavity FP interferometer based on serially splicing C-fibre between single mode fibres. A sensitivity of 2200 nm/RIU was achieved with minimal crosstalk between the two cavities. In this project, the proposed sensors were first utilised for refractive index sensing during which the measurand information was obtained by a phase demodulation technique. After that, the multiplexing ability of the proposed sensors were demonstrated by cascading two C-shaped interferometers. The potential of using the proposed sensors as multiplexed biochemical sensors was studied by first coating both interferometers with polyelectrolyte nanofilms, followed by functionalising one of the interferometers with biotin molecules after which both interferometers were utilised for streptavidin sensing. The results demonstrated that the proposed sensors can potentially act as a quantitative biochemical sensor in the future. In this project, the utilisation of C-shaped fibres offers a simple way for the measurand to directly interact with the light path. By using the dual interferometer system for multiplexed sensing, the proposed sensor has the ability to simultaneously measure a target parameter and a negative control. This can significantly reduce false positive measurements. Future work can focus on expanding the multiplexing capability of the sensor system and applying the technique to biochemical targets of interest, such as viruses and bacteria.

The optical fibre dye lasers were explored with both C-shaped fibres and ECF providing interaction between the propagating light and the gain medium. Simulations and calculations of the C-shaped fibre cavity and ECF cavity were conducted to assess the feasibility. With the Beer-Lambert law, the optimal dye concentration and length were calculated to obtain reasonable pump laser absorption as well as low lasing threshold. By using the microcavities fabricated with C-shaped fibre and ECF, the dye solution can be efficiently circulated by an external peristaltic pump. This solves a critical problem of dye lasers, which is how to avoid dye photobleaching but without requiring large quantities of dye solution. Using the proposed laser configuration, a clear fluorescence spectrum was obtained in both CW mode and pulsed mode of the pumping laser based on C-shaped fibre cavity. In addition, during the experiments with the C-shaped fibre cavity, a Raman laser operation was observed, which came from the long multimode fibres. In this project, the beam quality of the pump laser, the coupling efficiency between the lead-in/out fibres significantly limits the laser results, which can be further solved by optimising fabrication process and using alternate pump sources. In addition, wavelength selection components can be added to the setup to ensure that Raman lasing can be suppressed and lasing at the fluorescence band can be obtained.

References

[1] K. C. Kao and G. A. Hockham, "Dielectric-fibre surface waveguides for optical frequencies," *IEE Proceedings-J Optoelectronics,* vol. 113, no. 7, pp. 1151-1158, 1966.

[2] A. W. Snyder and J. D. Love, *Optical waveguide theory*. USA: Chapman and Hall, 1983.

[3] L. Xie, L. V. Nguyen, H. Ebendorff-Heidepriem, and S. C. Warren-Smith, "Multiplexed optical fiber biochemical sensing using cascaded C-shaped Fabry-Perot Interferometers," *IEEE Sensor Journal,* vol. 19, no. 22, 2019.

[4] C. Wu, Z. Liu, A. Zhang, B. Guan, and H. Tam, "In-line open-cavity Fabry–Pérot interferometer formed by C-shaped fiber fortemperature-insensitive refractive index sensing," *Optics Express,* vol. 22, no. 18, pp. 21757-21766, 2014.

[5] S. Weng, L. Pei, J. Wang, T. Ning, and J. Li, "High sensitivity D-shaped hole fiber temperature sensor based on surface plasmon resonance with liquid filling," *Photonics Research,* vol. 5, no. 2, pp. 103-107, 2017.

[6] Y. Lo, C. Chuang, and Z. Lin, "Ultrahigh sensitivity polarimetric strain sensor based upon D-shaped optical fiber and surface plasmon resonance technology," *Optics letters,* vol. 36, no. 13, pp. 2489-2491, 2011.

[7] C. Chen, T. Tsao, J. Tang, and W. Wu, "A multi-D-shaped optical fiber for refractive index sensing," *Sensors,* vol. 10, no. 5, pp. 4794-4804, 2010.

[8] N. Luan, R. Wang, W. Lv, and J. Yao, "Surface plasmon resonance sensor based on D-shaped microstructured optical fiber with hollow core," *Optics Express,* vol. 23, no. 7, pp. 8576-8582, 2015.

[9] R. B. Dyott, J. Bello, and V. A. Handerek, "Indium-coated D-shaped-fiber polarizer," *Optics letters,* vol. 12, no. 4, pp. 287-289, 1987.

[10] L. Jiang, L. Zhao, S. Wang, J. Yang, and H. Xiao, "Femtosecond laser fabricated all-optical fiber sensors with ultrahigh refractive index sensitivity: modeling and experiment," *Optics express,* vol. 19, no. 18, pp. 17591-17598, 2011.

[11] S. A. Cerqueira, "Recent progress and novel applications of photonic crystal fibers," *Reports on Progress in Physics,* vol. 73, no. 2, 2010.

[12] P. Russell, "Photonic crystal fibers," *Science,* vol. 299, no. 5605, pp. 358-362, 2003.

[13] J. C. Knight, T. A. Birks, P. S. J. Russell, and D. M. Atkin, "All-silica single-mode optical fiber with photonic crystal cladding," *Optics Letters,* vol. 21, no. 19, p. 1547, 1996.

[14] P. Russell, "Photonic-Crystal fibers," *Journal of Lightwave Technology,* vol. 24, no. 12, pp. 4729-4749, 2006.

[15] T.T. Alkeskjold *et al.*, "Photonic crystal fiber amplifiers for high power ultrafast fiber lasers," *Nanophotonics,* vol. 2, no. 5-6, pp. 369-382, 2013.

[16] O. Frazão, J. Santos, F. M. A. jo, and L. A. Ferreira, "Optical sensing with photonic crystal fibers," *Laser and Photonics Review,* vol. 2, no. 6, pp. 449-459, 2008.

[17] J. M. Dudley, G. Genty, and S. Coen, "Supercontinuum generation in photonic crystal fiber," *Reviews of Modern Physics,* vol. 78, pp. 1135-1176, 2006.

[18] D. K. C. Wu, B. T. Kuhlmey, and B. J. Eggleton, "Ultrasensitive photonic crystal fiber refractive index sensor," *Optics letters,* vol. 34, no. 3, pp. 322-324, 2009.

[19] J. B. Jensen *et al.*, "Photonic crystal fiber based evanescent-wave sensor for detection of biomolecules in aqueous solutions," *Optics letters,* vol. 29, no. 17, pp. 1974-1976, 2004.

[20] L. Rindorf, J. B. Jensen, M. Dufva, L. H. Pedersen, P. E. Hoiby, and O. Bang, "Photonic crystal fiber long-period gratings for biochemical sensing," *Optics express,* vol. 14, no. 18, pp. 8824-8831, 2006.
[21] N. Skivesen, A. Tetu, M. Kristensen, J. Kjems, L. H. Frandsen, and P. I. Borel, "Photonic-crystal waveguide biosensor," *Optics express,* vol. 15, no. 6, pp. 3169-3176, 2007.
[22] S. C. Warren-Smith, L. V. Nguyen, C. Lang, H. Ebendorff-Heidepriem, and T. M. Monro, "Temperature sensing up to 1300° C using suspended-core microstructured optical fibers," *Optics express,* vol. 24, no. 4, pp. 3714-3719, 2016.
[23] S. C. Warren-Smith, E. Sinchenko, P. R. Stoddart, and T. M. Monro, "Distributed fluorescence sensing using exposed core microstructured optical fiber," *IEEE Photonics Technology Letters,* vol. 22, no. 18, pp. 1385-1387, 2010.
[24] S. Afshar, S. C. Warren-Smith, and T. M. Monro, "Enhancement of fluorescence-based sensing using microstructured optical fibres," *Optics express,* vol. 15, no. 26, pp. 17891-17901, 2007.
[25] X. Li, L. V. Nguyen, Y. Zhao, H. Ebendorff-Heidepriem, and S. C. Warren-Smith, "High-sensitivity Sagnac-interferometer biosensor based on exposed core microstructured optical fiber," *Sensors & Actuators: B. Chemical,* vol. 269, pp. 103-109, 2018.
[26] S. C. Warren-Smith and T. M. Monro, "Exposed core microstructured optical fiber Bragg gratings: refractive index sensing," *Optics express,* vol. 22, no. 2, pp. 1480-1489, 2014.
[27] T. M. Monro *et al.*, "Sensing with suspended-core optical fibers," *Optical Fiber Technology,* vol. 16, no. 6, pp. 343-356, 2010.
[28] K. O. Hill, Y. Fujii, D. C. Johnson, and B. S. Kawasaki, "Photosensitivity in optical fiber waveguides: application to reflection filter fabrication," *Applied Physics Letters,* vol. 32, no. 10, pp. 647-649, 1978.
[29] G. Meltz, W. W. Morey, and W. H. Glenn, "Formation of Bragg gratings in optical fibers by a transverse holographic method," *Optics Letters,* vol. 14, no. 15, pp. 823-825, 1989.
[30] K. O. Hill and G. Meltz, "Fiber Bragg grating technology fundamentals and overview," *Journal of Lightwave Technology,* vol. 15, no. 8, pp. 1263-1276, 1997.
[31]V. Bhatia and A. M. Vengsarkar, "Optical fiber long-period grating sensors," *Optics Letters,* vol. 21, no. 9, pp. 692-694, 1996.
[32] J. Canning, "Fibre gratings and devices for sensors and lasers," *Laser and Photonics Review,* vol. 2, no. 4, 2008.
[33] J. Albert, L. Y. Shao, and C. Caucheteur, "Tilted fiber Bragg grating sensors," *Laser and Photonics Review,* vol. 7, no. 1, pp. 83-108, 2012.
[34] W. H. Loh, F. Q. Zhou, and J. J. Pan, "Sampled fiber grating based-dispersion slope compensator," *IEEE Photonics Technology Letters,* vol. 11, no. 10, pp. 1280-1282, 1999.
[35] C. R. Giles, "Lightwave applications of fiber Bragg gratings," *Journal of Lightwave Technology,* vol. 15, no. 8, pp. 1391-1404, 1997.
[36] A. N. Chryssis, S. S. Saini, S. M. Lee, H. Yi, W. E. Bentley, and M. Dagenais, "Detecting hybridization of DNA by highly sensitive evanescent field etched core fiber Bragg grating sensors," *IEEE Journal of Selected Topics in Quantum Electronics,* vol. 11, no. 4, pp. 864-872, 2005.
[37] S. Sridevi, K. S. Vasu, S. Asokan, and A. K. Sood, "Sensitive detection of C-reactive protein using optical fiber Bragg gratings," *Biosensors and Bioelectronics,* vol. 65, pp. 251-256,

2015.
[38] S. Schulze, M. Wehrhold, and C. Hille, "Femtosecond-Pulsed Laser Written and Etched Fiber Bragg Gratings for Fiber-Optical Biosensing," *Sensors,* vol. 18, no. 9, pp. 2844-2863, 2018.
[39] S. C. Warren-Smith and T. M. Monro, "Exposed core microstructured optical fiber Bragg gratings: refractive index sensing," *Optics express,* vol. 22, no. 2, 2014.
[40] R. C. Jorgenson and S. S. Yee, "A fiber-optic chemical sensor based on surface plasmon resonance," *Sensors & Actuators: B-Chemical,* vol. 12, no. 3, pp. 213-220, 1993.
[41] L.-K. Chau, Y.-F. Lin, S.-F. Cheng, and T.-J. Lin, "Fiber-optic chemical and biochemical probes based on localized surface plasmon resonance," *Sensors & Actuators: B. Chemical,* vol. 113, no. 1, pp. 100-105, 2006.
[42] A. Hassani and M. Skorobogatiy, "Design of the microstructured optical fiber-based surface plasmon resonance sensors with enhanced microfluidics," *Optics express,* vol. 14, no. 24, pp. 11616-11621, 2006.
[43] S. Gao *et al.*, "High-sensitivity DNA biosensor based on microfiber Sagnac interferometer," *Optics express,* vol. 25, no. 12, pp. 13305-13313, 2017.
[44] S. C. Warren-Smith, R. M. Andre, J. Dellith, T. Eschrich, M. Becker, and H. Bartelt, "Sensing with ultra-short Fabry-Perot cavities written into optical micro-fibers," *Sensors & Actuators: B. Chemical,* vol. 244, pp. 1016-1021, 2017.
[45] Y. Zhang, X. Chen, Y. Wang, K. L. Cooper, and A. Wang, "Microgap multicavity Fabry–Pérot biosensor," *Journal of Lightwave Technology,* vol. 25, no. 7, pp. 1797-1804, 2007.
[46] C. R. Liao, T. Y. Hu, and D. N. Wang, "Optical fiber Fabry-Perot interferometer cavity fabricated by femtosecond laser micromachining and fusion splicing for refractive index sensing," *Optics Express,* vol. 20, no. 20, pp. 22813-22818, 2012.
[47] D. Duan, Y. Rao, and T. Zhu, "High sensitivity gas refractometer based on all-fiber open-cavity Fabry-Perot interferometer formed by large lateral offset splicing," *Journal of the Optical Society of America B: Optical Physics,* vol. 29, no. 5, pp. 912-915, 2012.
[48] W. T. Silfvast, *Laser fundamentals*. United Kingdom: Cambridge University Press, 2004.
[49] R. R. Gattass and E. Mazur, "Femtosecond laser micromachining in transparent materials," *Nature Photonics,* vol. 2, pp. 219-225, 2008.
[50] O. Svelto, *Principles of lasers*. Springer, 1998.
[51] O. G. Okhotnikov, *High-power fiber lasers and Fiber lasers*. Germany: Wiley-VCH, 2013.
[52] J. T. Verdeyen, *Laser Electronics*. New Jersey: Prentice Hall, 1994.
[53] C. J. Koester and E. Snitzer, "Amplification in a fiber laser," *Appied Optics,* vol. 3, no. 10, pp. 1182-1186, 1964.
[54] D. J. Richardson, J. Nilsson, and W. A. Clarkson, "High power fiber lasers: current status and future perspectives," *Journal of Optical Society of America-B,* vol. 27, no. 11, pp. B63-B92, 2010.
[55] C. Jauregui, J. Limpert, and A. Tunnermann, "High-power fibre lasers," *Nature Photonics,* vol. 7, pp. 861-867, 2013.
[56] M. E. Fermann and I. Hartl, "Ultrafast fibre lasers," *Nature Photonics,* vol. 7, pp. 868-874, 2013.
[57] M. N. Zervas and C. A. Codemard, "High power fiber lasers: a review," *IEEE Journal of Selected Topics in Quantum Electronics,* vol. 20, no. 5, 2014.

[58] S. D. Jackson, "Towards high-power mid-infrared emission from a fibre laser," *Nature Photonics,* vol. 6, pp. 423-431, 2012.
[59] L. He, S. K. Ozdemir, and L. Yang, "Whispering gallery microcavity lasers," *Laser and Photonics Reviews,* vol. 7, no. 1, pp. 60-82, 2013.
[60] P. Urquhapt, "Review of rare-earth doped fiber lasers and amplifiers," *IEE Proceedings-J Optoelectronics,* vol. 135, no. 6, pp. 385-402, 1988.
[61] J. Canning, "Fibre lasers and related technologies," *Optics and Lasers in Engineering,* vol. 44, no. 7, pp. 647-676, 2006.
[62] C. R. Giles and E. Desurvire, "Modelling erbium-doped fiber amplifiers," *Journal of Lightwave Technology,* vol. 9, no. 2, pp. 271-283, 1991.
[63] E. M. Dianov, V. V. Dvoyrin, V. M. Mashinsky, A. A. Umnikov, M. V. Yashkov, and A. N. Gur'yanov, "CW bismuth fibre laser," *Quantum Electronics,* vol. 35, no. 12, pp. 1083-1084, 2005.
[64] Y. Jeong, J. K. Sahu, D. N. Payne, and J. Nilsson, "Ytterbium-doped large-core fiber laser with 1.36 kW continuous-wave output power," *Optics Express,* vol. 12, no. 5, pp. 6088-6092, 2004.
[65] M. A. Solodyankin *et al.*, "Mode-locked 1.93μm thulium fiber laser with a carbon nanotube absorber," *Optics Letters,* vol. 33, no. 12, pp. 1336-1338, 2008.
[66] I. A. Bufetov and E. M. Dianov, "Bi-doped fiber lasers," *Laser Physics Letters,* vol. 6, no. 7, pp. 487-504, 2009.
[67] F. P. Schafer, B. B. Snavely, C. V. Shank, E. P. Ippen, K. H. Drexhage, and T. W. Hansch, *Dye lasers*. German: Springer, 1973.
[68] D. L. Stockman, W. R. Mallory, and K. F. Tittel, "Stimulated emission in aromatic organic compounds," in *Proceedings of IEEE*, 1964.
[69] G. J. Pendock, H. S. MacKenzie, and F. P. Payne, "Dye lasers using tapered optical fibers," *Applied Optics,* vol. 32, no. 27, pp. 5236-5242, 1993.
[70] R. M. Gerosa, Z. Sudirman, L. D. S. Menezes, W. Margulis, and C. J. S. D. Matos, "All-fiber high repetition rate microfluidic dye laser," *Optica,* vol. 2, no. 2, pp. 186-193, 2015.
[71] H. Zhou, G. Feng, K. Yao, C. Yang, J. Yi, and S. Zhou, "Fiber-based tunable microcavity fluidic dye laser," *Optics Letters,* vol. 38, no. 18, pp. 3604-3607, 2013.
[72] Z. Li, W. Zhou, M. Luo, Y. Liu, and J. Tian, "Tunable optofluidic microring laser based on a tapered hollow core microstructured optical fiber," *Optics Express,* vol. 23, no. 8, pp. 10413-10420, 2015.
[73] X. Fu, P. Lu, W. Ni, H. Liao, D. Liu, and J. Zhang, "Phase demodulation of interferometric fiber sensor based on fast Fourier analysis," *Optics Express,* vol. 25, no. 18, pp. 21094-21106, 2017.
[74] C. C. Katsidis and D. I. Siapkas, "General transfer-matrix method for optical multilayer systems with coherent, partially coherent, and incoherent interference," *Appied Optics,* vol. 41, no. 19, pp. 3978-3987, 2002.
[75] S. C. Warren-Smith, R. Kostecki, L. V. Nguyen, and T. M. Monro, "Fabrication, splicing, Bragg grating writing, and polyelectrolyte functionalization of exposed-core microstructured optical fibers," *Optics Express,* vol. 22, no. 24, pp. 29493-29504, 2014.
[76] E. P. Schartner, A. Dowler, and H. Ebendorff-Heidepriem, "Fabrication of low-loss, small-core exposed core microstructured optical fibers," *Optical Materials Express,* vol. 7, no. 5, pp.

1496-1502, 2017.
[77] S. C. Warren-Smith, S. Afshar, and T. M. Monro, "Theoretical study of liquid-immersed exposed-core microstructured optical fibers for sensing," *Optics Express,* vol. 16, no. 12, pp. 9034-9045, 2008.
[78] K. Hayata, M. Koshiba, and M. Suzuki, "Modal spot size of axially nonsymmetrical fibres," *Electronics Letters,* vol. 22, no. 3, pp. 127-129, 1986.
[79] *Damage threshold of optical fibre*. Available: https://www.thorlabs.com/newgrouppage9.cfm?objectgroup_id=334
[80] L. F. Mottram, S. Forbes, B. D. Ackley2, and B. R. Peterson, "Hydrophobic analogues of rhodamine B and rhodamine 101: potent fluorescent probes of mitochondria in living C. elegans," *Beilstein Journal of Organic Chemistry,* vol. 8, no. 1, pp. 2156-2165, 2012.
[81] D. Beer and J. Weber, "Photobleaching of organic laser dyes," *Optics Communication,* vol. 5, no. 4, pp. 307-309, 1972.
[82] R. M. Gerosa, A. Sudirman, L. d. S. Menezes, W. Margulis, and C. J. S. d. Matos, "All-fiber high repetition rate microfluidic dye laser," *Optica,* vol. 2, no. 2, pp. 186-193, 2015.